The Astrophysical Journal, 964:24 (21pp), 2024 March 20 https://doi.org/10.3847/1538-4357/ad1f57

Early Planet Formation in Embedded Disks (eDisk). XIV. Flared Dust Distribution and Viscous Accretion Heating of the Disk around R CrA IRS 7B-a

Shigehisa Takakuwa[1,2], Kazuya Saigo[1], Miyu Kido[1,2], Nagayoshi Ohashi[2], John J. Tobin[3], Jes K. Jørgensen[4], Yuri Aikawa[5], Yusuke Aso[6], Sacha Gavino[4], Ilseung Han[6,7], Patrick M. Koch[2], Woojin Kwon[8,9], Chang Won Lee[6,7], Jeong-Eun Lee[10], Zhi-Yun Li[11], Zhe-Yu Daniel Lin[11], Leslie W. Looney[3,12], Shoji Mori[13], Jinshi Sai (Insa Choi)[2], Rajeeb Sharma[4], Patrick D. Sheehan[3], Kengo Tomida[13], Jonathan P. Williams[14], Yoshihide Yamato[5], and Hsi-Wei Yen[2]

[1] Department of Physics and Astronomy, Graduate School of Science and Engineering, Kagoshima University, 1-21-35 Korimoto, Kagoshima, Kagoshima 890-0065, Japan; takakuwa@sci.kagoshima-u.ac.jp
[2] Academia Sinica Institute of Astronomy & Astrophysics, 11F of Astronomy-Mathematics Building, AS/NTU, No.1, Sec. 4, Roosevelt Road, Taipei 10617, Taiwan, ROC
[3] National Radio Astronomy Observatory, 520 Edgemont Road, Charlottesville, VA 22903, USA
[4] Niels Bohr Institute, University of Copenhagen, Øster Voldgade 5–7, DK 1350 Copenhagen K., Denmark
[5] Department of Astronomy, Graduate School of Science, The University of Tokyo, 7-3-1 Hongo, Bunkyo-ku, Tokyo 113-0033, Japan
[6] Korea Astronomy and Space Science Institute, 776 Daedeok-daero, Yuseong-gu, Daejeon 34055, Republic of Korea
[7] Division of Astronomy and Space Science, University of Science and Technology, 217 Gajeong-ro, Yuseong-gu, Daejeon 34113, Republic of Korea
[8] Department of Earth Science Education, Seoul National University, 1 Gwanak-ro, Gwanak-gu, Seoul 08826, Republic of Korea
[9] SNU Astronomy Research Center, Seoul National University, 1 Gwanak-ro, Gwanak-gu, Seoul 08826, Republic of Korea
[10] Department of Physics and Astronomy, Seoul National University, 1 Gwanak-ro, Gwanak-gu, Seoul 08826, Republic of Korea
[11] University of Virginia, 530 McCormick Road, Charlottesville, VA 22904, USA
[12] Department of Astronomy, University of Illinois, 1002 West Green Street, Urbana, IL 61801, USA
[13] Astronomical Institute, Graduate School of Science, Tohoku University, Sendai 980-8578, Japan
[14] Institute for Astronomy, University of Hawai'i at Mānoa, 2680 Woodlawn Drive, Honolulu, HI 96822, USA

Received 2023 November 12; revised 2024 January 10; accepted 2024 January 15; published 2024 March 12

Abstract

We performed radiative transfer calculations and observing simulations to reproduce the 1.3 mm dust-continuum and $C^{18}O$ (2–1) images in the Class I protostar R CrA IRS7B-a, observed with the ALMA Large Program "Early Planet Formation in Embedded Disks (eDisk)." We found that a dust disk model passively heated by the central protostar cannot reproduce the observed peak brightness temperature of the 1.3 mm continuum emission (∼195 K), regardless of the assumptions about the dust opacity. Our calculation suggests that viscous accretion heating in the disk is required to reproduce the observed high brightness temperature. The observed intensity profile of the 1.3 mm dust-continuum emission along the disk minor axis is skewed toward the far side of the disk. Our modeling reveals that this asymmetric intensity distribution requires flaring of the dust along the disk vertical direction with the scale height following $h/r \sim r^{0.3}$ as a function of radius. These results are in sharp contrast to those of Class II disks, which show geometrically flat dust distributions and lower dust temperatures. From our modeling of the $C^{18}O$ (2–1) emission, the outermost radius of the gas disk is estimated to be ∼80 au, which is larger than that of the dust disk (∼62 au), to reproduce the observed distribution of the $C^{18}O$ (2–1) emission in IRS 7B-a. Our modeling unveils a hot and thick dust disk plus a larger gas disk around one of the eDisk targets, which could be applicable to other protostellar sources in contrast to more evolved sources.

Unified Astronomy Thesaurus concepts: Interstellar medium (847); Planet formation (1241); Radiative transfer (1335); Star formation (1569)

1. Introduction

The ALMA Large Program "Early Planet Formation in Embedded Disk (eDisk)" has newly observed 11 Class 0 and 6 Class I protostars in 1.3 mm dust continuum and selected molecular lines, including $C^{18}O$ (2–1), around 230 GHz at a spatial resolution of ∼7 au (plus one Class 0 and I source each from archival data). The data sets enable us to systematically investigate the ongoing disk and planet formation occurring during the protostellar stages (Ohashi et al. 2023). As reported in the present series of the eDisk first-look papers, the initial results have demonstrated intriguing features of the protostellar disks, envelopes, and outflows. For example, eDisk has unveiled that Keplerian-rotating disks are often found even in the Class 0 stage (Aso et al. 2023; Hoff et al. 2023; Kido et al. 2023; Sai et al. 2023; Sharma et al. 2023; Thieme et al. 2023). Concentric ring and gap features that are often seen in Class II disks (e.g., Andrews et al. 2018), on the other hand, are only seen toward the most evolved eDisk sources Oph IRS 63 (Flores et al. 2023) and L1489 IRS (Yamato et al. 2023), and so-called bump or shoulder features are seen in the Class 0 sources Ced 110 IRS 4 (Sai et al. 2023) and CB 68 (Kido et al. 2023). In the envelopes, flow-like molecular gas accreting toward the central protostellar disks, accretion streamers, has been identified (I. Han et al. 2023, in preparation; Aso et al. 2023; Flores et al. 2023; Kido et al. 2023). An extended circumbinary envelope around the compact binary disks is also identified (Narayanan et al. 2023).

To place these observational results into a quantitative astrophysical context, we need to compare the observations to

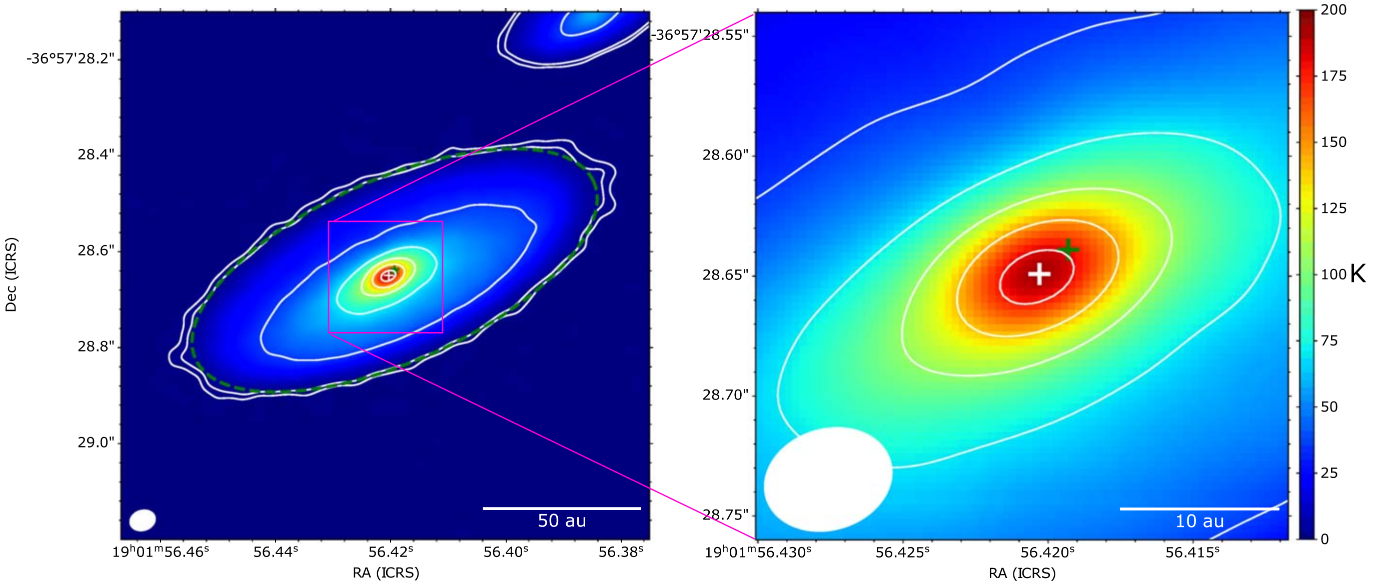

Figure 1. Overall (left) and zoom-in images (right) of the observed 1.3 mm dust-continuum emission in IRS 7B-a. The solid contours show 5σ, 9σ, 100σ, 200σ, 300σ, 400σ, and 500σ ($1\sigma = 0.033$ mJy beam^{-1} = 0.36 K). The beam size is $0\overset{''}{.}054 \times 0\overset{''}{.}042$ (P.A. = $-72\overset{\circ}{.}6$). The white cross denotes the peak position of the 1.3 mm dust-continuum emission, whose coordinates are $(19^{\rm h}01^{\rm m}56\overset{\rm s}{.}420, -36^{\circ}57'28\overset{''}{.}65)$. This position is adopted as the origin of the intensity profile and the PV diagrams. For reference, the green cross is the approximate geometrical center of the ellipse (dashed green line), which delineates the contour with an intensity of 0.3 mJy beam^{-1}.

detailed synthetic observations based on radiative transfer modeling of protostellar disks and envelopes (see Baek et al. 2020) properly processed with simulations of the ALMA imaging process. In this paper, we report our first attempt to reproduce the observed 1.3 mm continuum and C^{18}O (2–1) emission in one of the eDisk targets, R CrA IRS 7B (Groppi et al. 2007; Peterson et al. 2011; Lindberg & Jørgensen 2012; Lindberg et al. 2014a, 2014b). R CrA IRS 7B is a Class I protostar located in Corona Australis, with a bolometric luminosity of $L_{\rm bol} = 5.1\ L_{\odot}$ and a bolometric temperature of $T_{\rm bol} = 88$ K, which were reestimated using the archival photometric data by the eDisk team (see Ohashi et al. 2023, for details). Note that both in terms of its bolometric luminosity and temperature, R CrA IRS 7B is typical of the eDisk targets. The distance to the source is estimated to be 152 pc based on the GAIA data (Galli et al. 2020). Previous SMA and ALMA observations of R CrA IRS 7B demonstrated the presence of compact 1.3 and 0.8 mm continuum emission (Lindberg & Jørgensen 2012; Lindberg et al. 2014b; Perotti et al. 2023). Through ALMA observations of the C^{17}O (3–2) line, a velocity gradient along the major axis of the dust emission was identified, which is interpreted as the signature of Keplerian rotation (Lindberg et al. 2014b). The angular resolutions of these previous observations are, however, not sufficient to investigate the detailed internal structure of the protostellar disk. The eDisk observations revealed for the first time that R CrA IRS 7B consists of two sources: one to the southeast (R CrA IRS 7B-a), and the other to the northwest (R CrA IRS 7B-b). Each source is surrounded by a separate dust disk (Ohashi et al. 2023). In the present paper, we focus on the southeastern source, R CrA IRS 7B-a, which is referred to as IRS 7B-a hereafter.

Figure 1 shows the entire and zoom-in views of the observed 1.3 mm dust-continuum emission in IRS 7B-a (Ohashi et al. 2023). The peak brightness temperature of the 1.3 mm dust-continuum emission is as high as ∼195 K. It is clear that along the minor axis, the emission gradient toward the northeast is steeper than toward the southwest, suggesting an asymmetry (Figure 1 right). Ohashi et al. (2023) also found that the C^{18}O (2–1) emission shows a signature of Keplerian rotation in the disk with an inferred central protostellar mass of 2.1–3.2 $M_{\odot}$, while the emission becomes weaker at the disk center against the bright dust-continuum emission.

Similar characteristics are also seen in several other eDisk sources, and it is therefore important to reproduce these features with radiative transfer modeling and to study the physical causes of these characteristics. Our approach, however, is not to construct elaborate theoretical models of the protostellar system or to perform a quantitative fitting of the model to the observed images. Instead, we aim to construct a simple but sufficient physical model that can reproduce these observed characteristic features as quantitatively as possible. This approach enables us to discuss the primary causes of the observed features and the important insights we can gain from them.

The structure of the present paper is as follows. In Section 2 the physical models of the disk and envelope are described, followed by a detailed explanation of the radiative transfer calculations and the model parameter search. In Section 3 the model images of the 1.3 mm dust-continuum emission with a range of model parameters are compared to the real observed 1.3 mm image. The physical causes of the high observed brightness temperature of the 1.3 mm dust-continuum emission and the asymmetric intensity profile along the disk minor axis are discussed separately. In Section 4 the model C^{18}O velocity channel maps and position-velocity (PV) diagrams are compared to those of the real data. In Section 5 we discuss the implications of our modeling results in the context of the evolution of disks into planet formation. Section 6 gives a concise summary of the present work.

2. Model

We introduce protostellar disk + envelope models that should be able to capture the main observed features with the minimum model complexity. The gas and dust distributions are assumed to be azimuthally symmetric and mirror-symmetric with respect to the midplane. The spatial grids in a spherical polar coordinate system are $(r, \theta, \phi) = (512, 512, 1)$. In the radial direction, an equally spaced grid on a logarithmic scale is adopted. In the polar direction, a linearly equally spaced grid is adopted. In our preliminary parameter search, a coarser grid of (256, 256, 1) is also adopted for efficient calculations. The radius r and elevation angle θ are $r = 1.0$–20,000 au and $\theta = 0°$–90°. The innermost radius of 1 au is fine enough for the spatial resolution of the observed images (∼7 au). An even smaller inner radius makes the gas temperature too high and the collisional coefficients of $C^{18}O$ unavailable. Within this defined space, our model includes three distinct components: a Keplerian disk, a rotating and infalling protostellar envelope surrounding the disk, and a static cocoon of molecular gas surrounding the envelope. The cocoon is a spherical shell with a constant gas density of 10^4 cm^{-3} between $r = 10{,}000$ and 20,000 au that mimics the ambient molecular cloud component. No gas motion except for an isotropic turbulence of 0.2 km s^{-1} is included in the cocoon.

2.1. Keplerian Disk

The implementation of the Keplerian disk is similar to that by Kwon et al. (2015) and Ichikawa et al. (2021). The disk properties are calculated with the cylindrical radius R,

$$R = r \sin\theta. \tag{1}$$

The vertical scale height h_0 of dust and gas at $R = R_0$ is set to be

$$h_0 = \frac{c_{s_0}}{\Omega_{K_0}}, \tag{2}$$

where

$$c_{s_0} = \sqrt{\frac{k_B T_0}{m_p \mu}} \tag{3}$$

and

$$\Omega_{K_0} = \sqrt{\frac{G M_\star}{R_0^3}} \tag{4}$$

are the sound speed and the Keplerian angular velocity in the midplane, respectively, at a reference radius $R_0 = 1$ au, and where k_B denotes the Boltzmann constant, T_0 is the midplane dust temperature at R_0, m_p is the proton mass, μ (= 2.33) is the mean molecular weight, G is the gravitational constant, and $M_\star$ is the stellar mass. $M_\star$ is derived to be in the range of ~ 2.1–$3.2\,M_\odot$ from the analysis of the observed PV diagram in the $C^{18}O$ (2–1) emission (Ohashi et al. 2023), using the SLAM package (Aso & Sai 2023). In our model, $M_\star = 2.9$ $M_\odot$ is adopted, which provides a good match of the model velocity channel maps to the observed velocity channel maps in the $C^{18}O$ emission (see Section 4). We set $T_0 = 400$ K, which is simply adopted to calculate the scale height. The true gas and dust temperature are calculated later with a given density distribution. The radial profile of the scale height ($\equiv h(R)$), or the disk flaring, is expressed as

$$\frac{h(R)}{R} = \frac{h_0}{R_0}\left(\frac{R}{R_0}\right)^q, \tag{5}$$

where q denotes the disk-flaring index.

The gas surface density profile $\Sigma(R)$ is assumed to follow the power-law profile as

$$\Sigma(R) = \Sigma_0\left(\frac{R}{R_0}\right)^p, \tag{6}$$

where Σ_0 is the surface density at $R = R_0$, and p is the power-law index. p is normally assumed to be in the range between −0.5 and −1, and here $p = -0.5$ is adopted. The disk is sharply truncated at the inner spherical radius $r < r_{in}$ (= 1 au) and the outer radius $r > r_{gas}$. Σ_0 is then derived from the disk mass ($\equiv M_d$) as

$$\Sigma_0 = \frac{(2+p) R_0^p M_d}{2\pi (r_{gas}^{2+p} - r_{in}^{2+p})}. \tag{7}$$

The gas mass density ρ can be described as

$$\rho(R, z) = \frac{\Sigma(R)}{h(R)\sqrt{2\pi}} \exp\left(-\frac{1}{2}\left(\frac{z}{h(R)}\right)^2\right). \tag{8}$$

The velocity field in the disk is a simple Keplerian rotation, expressed as

$$v_\phi = \sqrt{\frac{G M_\star}{r}}. \tag{9}$$

The gas-to-dust mass ratio is assumed to be 100. During our modeling effort to reproduce both the 1.3 mm dust continuum and $C^{18}O$ (2–1) emission, we found, however, that the radius of the dust disk is likely smaller than that of the gas disk (see Section 4). Thus, we introduce an additional parameter, r_{dust}, the radius of the dust disk. Between r_{dust} and r_{gas}, the gas-to-dust mass ratio is arbitrarily enhanced by a factor of 50 to mimic a dust-free region of molecular gas (see Section 2.4). The $C^{18}O$ abundance is assumed to be the canonical value of 1.76×10^{-7} (Crapsi et al. 2004) and to be constant in the disk as well as in the envelope. As shown below, the calculated dust temperature in the disk is above the CO freeze-out temperature of 25 K in most parts of the disk, and thus, a constant CO abundance is a reasonable assumption.

2.2. Protostellar Envelope

In the radial range from r_{gas} to $r = 10{,}000$ au and above $z > 4 \times h$ at $r_{in} \leqslant r < r_{gas}$, the protostellar envelope of molecular gas and dust is filled. The gas-to-dust mass ratio is assumed to be 100 throughout the envelope as well as the cocoon. The choice of the vertical boundary between the disk and envelope at $4 \times h$ is somewhat arbitrary. If the boundary is set to be $1 \times h$, the model disk is too thin to show the effect of the disk flaring. We also note that the inclusion of the envelope component is important, even if the observed 1.3 mm dust-continuum and the $C^{18}O$ (2–1) emission appear to primarily trace the protostellar disk. As we show below, inclusion of viscous accretion heating is likely required to reproduce the intense 1.3 mm dust-continuum emission originating from the disk. The protostellar envelope should supply the accreting material to the disk. Furthermore, the presence of the protostellar envelope acts as a blanket for the disk by slowing down the escape of photons from the disk.

The model of the rotating and infalling protostellar envelope is taken from Ulrich (1976), Hartmann et al. (1994), and Mendoza et al. (2004). It is a ballistic solution to the two-body problem, with the envelope material following parabolic trajectories around the central protostar. The velocity vector in the three-dimensional space is expressed as

$$v_r = -\left(\frac{GM_\star}{r}\right)^{\frac{1}{2}}\left(1 + \frac{\cos\theta}{\cos\theta_0}\right)^{\frac{1}{2}}, \tag{10}$$

$$v_\theta = \left(\frac{GM_\star}{r}\right)^{\frac{1}{2}}\left(\frac{\cos\theta_0 - \cos\theta}{\sin\theta}\right)\left(1 + \frac{\cos\theta}{\cos\theta_0}\right)^{\frac{1}{2}}, \tag{11}$$

$$v_\phi = \left(\frac{GM_\star}{r}\right)^{\frac{1}{2}}\frac{\sin\theta_0}{\sin\theta}\left(1 - \frac{\cos\theta}{\cos\theta_0}\right)^{\frac{1}{2}}, \tag{12}$$

where θ_0 denotes the initial elevation angle of the infalling material. When the envelope material enters the disk boundary (see above), the material is assumed to be incorporated into the disk. In the case of the isotropic infall in the envelope, the above infalling velocity yields the expression of the envelope density,

$$\rho(r, \theta) = \rho_0\left(\frac{r}{r_{\mathrm{gas}}}\right)^{-\frac{3}{2}}\left(1 + \frac{\cos\theta}{\cos\theta_0}\right)^{-\frac{1}{2}} \times \left(3\frac{r_{\mathrm{gas}}}{r}\cos^2\theta_0 + 1 - \frac{r_{\mathrm{gas}}}{r}\right)^{-1}, \tag{13}$$

where

$$\rho_0 = \frac{\dot{M}}{4\pi}\sqrt{\frac{1}{GM_\star r_{\mathrm{gas}}^3}}, \tag{14}$$

and $\dot{M}$ indicates the mass-infall rate of the envelope. Note that given $M_\star$ and r_{gas}, the density structure of the envelope is uniquely determined by $\dot{M}$.

The formulation proposed by Hartmann et al. (1994) is adopted to express the flattening of the envelope as

$$\rho_{\mathrm{flat}}(r, \theta) = \frac{\eta_f}{\cosh^2(\eta_f\cos\theta_0)\tanh\eta_f}\rho(r, \theta), \tag{15}$$

where η_f represents the degree of flattening of the envelope. $\eta_f = 1$ denotes no flattening, i.e., $\rho_{flat}(r, \theta) = \rho(r, \theta)$, while higher values of η_f indicate a stronger flattening. We adopt $\eta_f = 2$, following Momose et al. (1998).

Figures 2(a) and (b) show distributions of the volume gas density $n_{\mathrm{H_2}}$ ($\mathrm{cm^{-3}}$) in the envelope plus the cocoon and the disk, respectively, of our fiducial model. Figure 2(c) shows the distribution of the dust density in the disk. The difference of the radii between the molecular and dust disks is presented. The envelope mass of the fiducial model is 0.062 $M_\odot$, in contrast with the disk gas mass of 0.41 $M_\odot$. The cocoon mass is 1.9 $M_\odot$.

2.3. Radiative Transfer Calculations

With these gas and dust density distibutions, radiative transfer calculations to produce images of the 1.3 mm dust-continuum and C^{18}O (2–1) emission are conducted using RADMC-3D (Dullemond 2012). The RADMC-3D calculations involve three separate steps: (1) thermal Monte Carlo simulations to obtain the spatial dust temperature distribution self-consistently, radiative transfer calculations to produce images of (2) the dust-continuum emission and (3) the emission from the C^{18}O (2–1) line. To perform the thermal Monte Carlo simulations, the properties of the central heating source (i.e., the protostar) must be specified, together with the number of photons, the wavelength-dependent dust opacity, and if necessary, the spatial distribution of the internal heating rate. RADMC-3D requires the flux density and radius to specify the central protostar in general. For simplicity, the radiation from the protostar is assumed to be blackbody radiation from a point source. In this case, RADMC-3D only requires the blackbody temperature. The relation between the blackbody temperature ($\equiv T_\star$) and the protostellar luminosity ($\equiv L_\star$) is expressed as

$$T_\star = \left(\frac{L_\star}{4\pi R_\star^2\sigma_{\mathrm{sb}}}\right)^{\frac{1}{4}}, \tag{16}$$

where $R_\star$ and σ_{sb} denote the protostellar radius and the Stefan–Boltzmann constant, respectively. $L_\star$ is set to be the bolometric luminosity of IRS 7B-a ($= 5.2\ L_\odot$)[15] and $R_\star = 1\ R_\odot$, which gives $T_\star = 8714$ K. We note that L_{bol} is not strictly the same as $L_\star$. L_{bol} is derived from the spectral energy distribution (SED) fitting over the near-IR (NIR) to millimeter wavelengths (Ohashi et al. 2023). The NIR emission originating from the protostellar sphere should be attenuated by the surrounding disk, envelope, and the ambient gas. On the other hand, the attenuated NIR radiation should be reemitted at longer wavelengths, and thus a total radiation energy L_{bol} is still a reasonable proxy of $L_\star$. To estimate the error of L_{bol}, we tried a new SED fitting using only the data points with the highest value at each wavelength (see Figure 9 in Ohashi et al. 2023). The derived L_{bol} is 8.3 $L_\odot$, which is an increase by ~60% from the adopted value of $L_{\mathrm{bol}} = 5.2\ L_\odot$. As shown below, this highest possible value of L_{bol} is still too low to reproduce the observed high brightness temperature of the 1.3 mm dust-continuum emission.

Note that with a given $L_\star$, $R_\star$ and $T_\star$ are degenerate, and a larger $R_\star$ yields lower $T_\star$. $R_\star = 1\ R_\odot$ is likely a lower limit of the protostellar radius, so $T_\star$ is likely an upper limit. The background of this parameter choice is the observed bright 1.3 mm dust-continuum emission. As we describe below, we have found that the observed bright 1.3 mm dust-continuum emission cannot be reproduced with the heating from the central protostar alone, and internal heating in the disk is likely required. As RADMC-3D only requires the central blackbody temperature to calculate the heating from the central protostar, we set this temperature to a high value. We also attempted even higher luminosities and thus higher blackbody temperatures in our parameter search.

The dust-mass opacity is also important, but rather uncertain. To convert the observed 1.3 mm flux densities into the dust masses, eDisk papers adopt the Beckwith opacity, which gives $\kappa_{1.3\ \mathrm{mm}} = 2.3\ \mathrm{cm^2\ g^{-1}}$ with $\beta = 1$ (Beckwith et al. 1990). This $\kappa_{1.3\ \mathrm{mm}}$ value is similar to the values inferred in the disks around the Class 0 source HH 212 mms (Lin et al. 2021) and the Class I source IRAS 04302 + 2247 (Lin et al. 2023a). The Beckwith opacity is similar to the opacity with a maximum grain size of 1 mm at millimeter wavelengths (Andrews et al. 2011; Birnstiel et al. 2018; Han et al. 2023). Another adopted opacity in our modeling is the so-called DSHARP opacity (Birnstiel et al. 2018). While a variety of DSHARP opacity

---

[15] During our modeling effort, the source bolometric luminosity derived by the eDisk team was 5.2 $L_\odot$, which was later updated to 5.1 $L_\odot$ (Ohashi et al. 2023). Since the small difference of the luminosity yields a negligible difference of the stellar radius from 1.0 $R_\odot$ to 0.99 $R_\odot$ to have the same $T_\star$, in the present paper, we adopt 5.2 $L_\odot$ as the canonical value of the stellar luminosity.

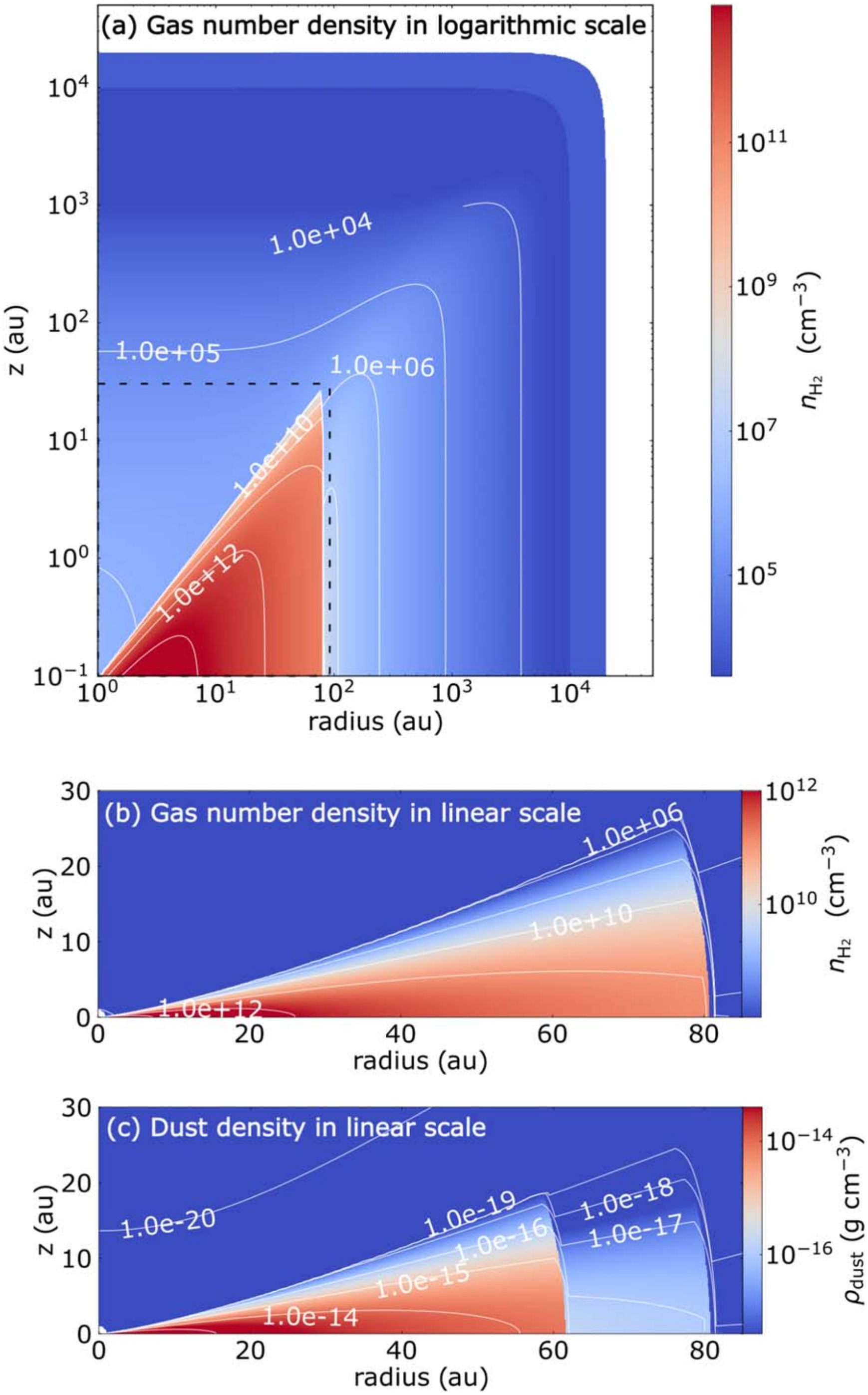

Figure 2. (a) Distribution of the gas number density ($\equiv n_{H_2}$) of the fiducial model in the log R-log z plane. The high-density region represents the disk, and the region outside the disk represents the protostellar envelope. In the outermost part of the envelope, a static uniform cocoon with $n_{H_2} = 10^4$ cm^{-3} is present. The contour levels start from 10^4 cm^{-3} in steps of a factor of 10. The dashed black rectangle delineates the zoom-in region shown in panels (b) and (c). (b) Zoom-in view of the n_{H_2} distribution in the disk region in the $R - z$ plane. The contour levels start from 10^6 cm^{-3} in steps of a factor of 10. (c) Same as panel (b), but for the distribution of the dust density, ρ_{dust}. Note the shorter outermost radius of the dust disk. The contour levels start from 10^{-20} g cm^{-3} in steps of a factor of 10.

tables can be obtained depending on the assumed dust parameters, the adopted DSHARP opacity in our models is the same as shown in the blue curve in Figure 6 by Birnstiel et al. (2018). The adopted opacity is an average over grain sizes from 0.1 μm to 1 mm with a power-law index of the grain size distribution of −3.5, where the grain composition is summarized in Table 1 in Birnstiel et al. (2018). In our parameter search, the Beckwith and DSHARP opacity were used mostly, but OH5 and Semenov opacities were also attempted (Figure 3). OH5 is the dust opacity taken from Table 1, Column 5, in Ossenkopf & Henning (1994). The dust model corresponds to grains that have coagulated at a gas density of 10^6 cm^{-3} with thin ice mantles from the initial MRN distribution (Mathis et al. 1977; Draine & Lee 1984). This has long been used as a standard opacity table for radiative transfer models and mass estimates for embedded protostars.

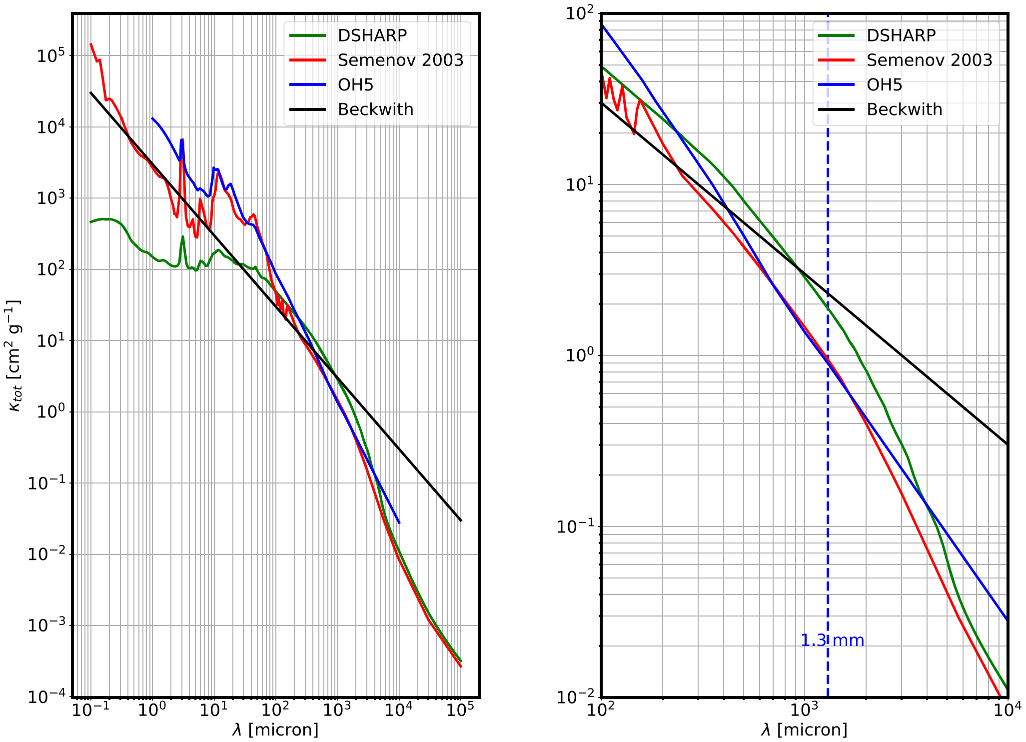

Figure 3. (Left) Dust-mass opacity (absorption and scattering) $\kappa_{\rm tot}$ (cm^2 g^{-1}) as a function of the wavelength of the four dust models: DSHARP, Semenov, OH5, and Beckwith. (Right) Zoom-in view of the left panel in the submillimeter and millimeter wavelength.

Regarding the Semenov opacity, the dust opacity table from Semenov et al. (2003) for the composite aggregate dust of the normal silicate mineralogy at $T < 155$ K is adopted.

In addition to the heating from the central protostar, we also incorporate the viscous accretion heating in the disk. The energy dissipation rate in the viscous Keplerian disk can be expressed as

$$q_{\rm heat} = \frac{9}{4}\rho\nu_{\rm vis}\Omega_{\rm K}^2, \tag{17}$$

where $\nu_{\rm vis}$ denotes the viscosity (Pringle 1981; D'Alessio et al. 1998). Assuming the constant $\nu_{\rm vis}$ along the disk vertical direction and steady accretion, the mass accretion rate $\dot{M}$ is

$$\dot{M} = 3\pi\Sigma\nu_{\rm vis}. \tag{18}$$

Substitution of Equation (18) into Equation (17) to remove $\nu_{\rm vis}$ yields

$$\begin{aligned} q_{\rm heat} &= \frac{9}{4}\rho\Omega_{\rm K}^2\frac{\dot{M}}{3\pi\Sigma} \\ &= \frac{3\dot{M}\Omega_K^2\rho(R,\,z)}{4\pi\Sigma(R)}. \end{aligned} \tag{19}$$

$\dot{M}$ is set to be the same as for the outer protostellar envelope. The α parameter can also be derived as

$$\alpha(R) = \frac{\nu_{\rm vis}}{c_s h} = \frac{\dot{M}}{3\pi\Omega_K(R)h(R)^2\Sigma(R)}. \tag{20}$$

Figure 4 shows the spatial distribution of the heating rate by the viscous accretion heating of the fiducial model. Figure 5 shows the radial profile of the α parameter in the fiducial model. The profile becomes a simple power law with a power-law index of -0.6. The α value of ∼0.01–0.1 is physically reasonable for a relatively young disk (e.g., Hu et al. 2022).

With the above setting, thermal Monte Carlo simulations are performed to calculate the spatial distributions of the dust temperature. To increase the computational speed, the modified random walk mode implemented in RADMC-3D is adopted, and the computation is performed in parallel with 30 threads. Then radiative transfer calculations to generate the model 1.3 mm dust-continuum images are made. For simplicity, we do not incorporate dust scattering in the radiative transfer calculations. Dust scattering suppresses the observed intensities (Yang et al. 2016, 2017; Lin et al. 2020; Yang & Li 2020; Lin et al. 2022, 2023a), while our model needs to explain the observed high brightness temperature of the 1.3 mm dust-continuum emission. Thus, inclusion of dust scattering does not change our conclusion that a dust disk passively heated by the central protostar alone cannot reproduce the observed brightness temperature.

Based on the assumption of equal dust and gas temperatures, radiative transfer calculations to generate the model C^{18}O (2–1) image cubes are also conducted. The LVG mode of RADMC-3D (i.e., linemode = 2) is adopted to calculate the non-LTE population distributions of C^{18}O, based on the assumption of a maximum photon escape length of 10 au. The C^{18}O rotational energy levels, transition frequencies, Einstein A-coefficients, and collisional coefficients with the ortho and para H$_2$ are taken from the Leiden Atomic and Molecular Database (LAMDA; Schöier et al. 2005).

After the radiative transfer calculations are completed, observing simulations are conducted to directly compare the model and observed images. The CASA task *ft* was used to sample the model images with the observed *uv* coverages of the IRS 7B data, and then the CASA task *tclean* was used to make the model images with the same imaging parameters as were

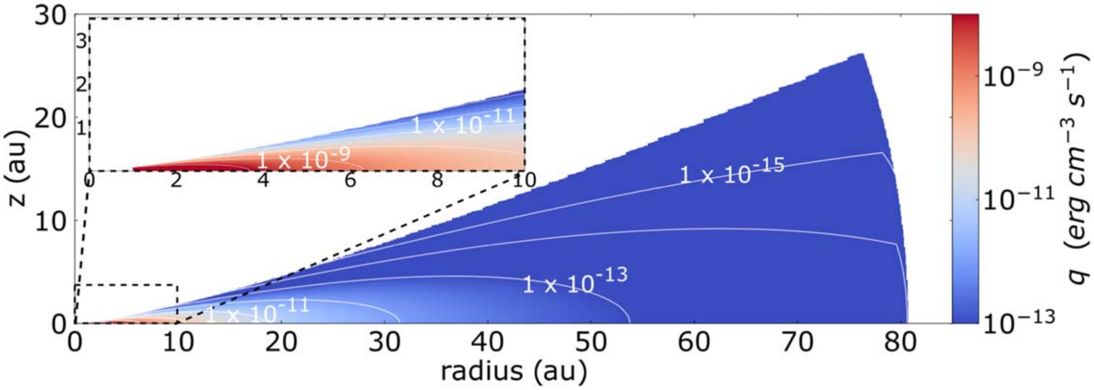

Figure 4. Distribution of the internal heating rate q_{heat} by the viscous accretion heating of the fiducial model, where $\dot{M} = 1.4 \times 10^{-6}$ ($M_{\odot}$ yr^{-1}). The contour levels start from 10^{-15} erg cm^{-3} s^{-1} in steps of a factor of 10.

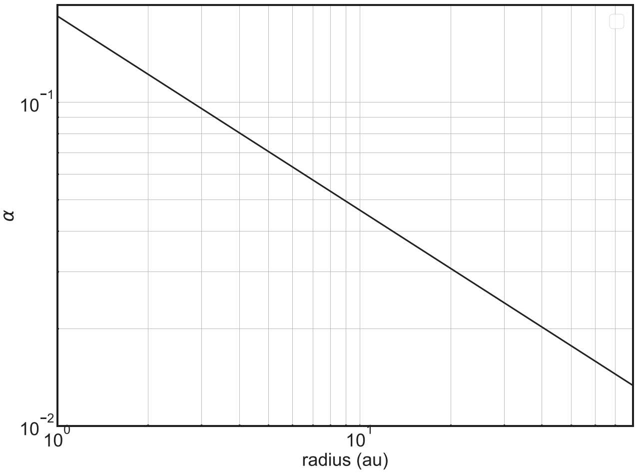

Figure 5. Radial distribution of the α parameter in the disk of the fiducial model.

used for the real observational data. In the case of the C^{18}O model, the sampled model visibility was continuum-subtracted with the CASA task *uvcontsub*, and then *tclean* was used to generate the line image cubes. Details of the imaging of the eDisk data are given by Ohashi et al. (2023).

2.4. Parameter Search

Our model requires a number of parameters and ALMA observing simulations, and thus substantial computational time. In addition, there is a possible offset of the peak position toward the southeast (Figure 1). The offset of the strong peak prevents us from calculating the numerical measure of the goodness of our axissymmetric model. Therefore, we do not adopt a numerical procedure to fit the model to the observed image such as a Markov Chain Monte Carlo (MCMC) method. Instead, we searched for model parameters that decently reproduce the observed images by eye. Comparisons between the models and observations were only performed on the image plane. This is because the image-based comparison is more intuitive, and the presence of the binary companion (IRS 7B-b) complicates the modeling of the visibilities. To reduce the dimension of the parameter space, we chose limited searching parameters, which we consider to directly affect the images and intensities. They include the disk mass (M_{d}), the gas and dust disk radii (r_{gas} and r_{dust}), the disk-flaring index q, the mass accretion rate ($\dot{M}$), the disk inclination angle (i), the protostellar luminosity ($L_{\star}$), and the dust mass opacity table. On the other hand, parameters such as the source distance, disk position angle, and the coordinates and wavelength of the observations are known a priori, and these parameters are fixed. The other fixed parameters are assumed to have canonical values often used in the literatures, or to be determined by the small preparatory parameter search (e.g., the protostellar mass $M_{\star} = 2.9$ $M_{\odot}$). The fixed parameters of the model are summarized in Table 1.

Table 1
Fixed Parameters for the IRS 7B-a Modeling

Parameter	Value
Radial Range	1–20,000 au
Distance	152 pc
Mass of the Protostar M_{*}	2.9 $M_{\odot}$
Radius of the Protostar R_{*}	1.0 $R_{\odot}$
Disk Position Angle θ_{d}	115°
Power-law Index of the Disk Surface Density p	−0.5
Temperature at 1 au	400 K
Envelope-flattening Factor η_f	2.0
Radial Range of the Static Cocoon	10,00–20,000 au
Gas Density of the Static Cocoon $n_{\mathrm{H_2}}^{\mathrm{coc}}$	10^4 cm^{-3}
Turbulent Velocity Dispersion in the Disk σ_{disk}	0.0 km s^{-1}
Turbulent Velocity Dispersion in the Envelope and Cocoon σ_{env}	0.2 km s^{-1}
Dust-continuum Wavelength	1.34 mm
C^{18}O Abundance $X_{\mathrm{C^{18}O}}^{\mathrm{can}}$	1.76×10^{-7}
Gas-to-Dust Mass Ratio ($r < r_{\mathrm{dust}}$, $r_{\mathrm{gas}} < r$)	100
Gas-to-Dust Mass Ratio ($r_{\mathrm{dust}} < r < r_{\mathrm{gas}}$)	5000
Ortho-to-Para Ratio of H$_2$	3.0
Photon-escaping Spatial Scale	10 au
Number of Photons	1.5×10^6

For the dust opacity table of Beckwith and DSHARP, we first tried to reproduce the extent and the aspect ratio of the observed image in the 1.3 mm dust-continuum emission and to adjust r_{dust}, M_{d}, and the inclination angle. Next, we reproduced the peak intensity of the continuum emission by adjusting $\dot{M}$ and M_{d}. We then checked that our choice of the power-law index of the radial surface density profile ($p = -0.5$) gives a decent radial intensity profile along the major axis. Next, we attempted to reproduce the observed skewed intensity profile along the minor axis. We found that the disk-flaring index q and M_{d} affect this most. As we discuss below, q and M_{d} are degenerate to reproduce the asymmetric intensity profile along the minor axis, and it is not straightforward to determine the best set of these two parameters. We adopt $M_d = 0.41\ M_\odot$ and $q = 0.3$, both of which appear to be reasonable, as fiducial values. For the dust opacity table of OH5 and Semenov, only a small parameter search around the fiducial values was performed. These additional searches revealed that the choice of the dust opacity table does not significantly affect the model 1.3 mm images.

Finally, with the given model image of the dust-continuum emission, we tried to reproduce the observed $C^{18}O$ image cube by changing r_{gas}. Here, we attempted several values of the enhanced gas-to-dust mass ratio between r_{dust} and r_{gas} and determined the fixed value of the gas-to-dust mass ratio of 5000. The enhancement of a factor of 50 of the gas-to-dust mass ratio was chosen to keep the dust temperature distribution flat. If the amount of the dust is further reduced, the dust temperature in that region increases. To verify that r_{gas} is larger than r_{dust}, we also changed r_{dust} and checked the resultant model $C^{18}O$ image cubes.

Our fiducial model is model 61 in Table 2 in the Appendix, where the disk-flaring index is $q = 0.30$, the gas +dust disk mass is $M_d = 0.41\ M_\odot$, the dust disk radius is $r_{dust} = 62$ au, the gas disk radius is $r_{gas} = 80$ au, the mass accretion rate is $\dot{M} = 1.4 \times 10^{-6}\ M_\odot\ \mathrm{yr}^{-1}$, the disk inclination is $i = -70°$, the central stellar luminosity is $L_\star = 5.2\ L_\odot$, and the DSHARP opacity is adopted. After the fiducial model parameters have been obtained, we changed one of the parameters to determine the dependence of that particular parameter, and those parameters include $L_\star$, M_d, q, and $\dot{M}$, i.e., inclusion or exclusion of the viscous accretion heating. All the varied model parameters are listed in Table 2.

3. Modeling of the 1.3 mm Dust-continuum Image

3.1. 1.3 mm Dust-continuum Intensity

We first aim to reproduce the observed bright 1.3 mm intensity in the protostellar disk around IRS 7B-a. Figure 6 shows the model 1.3 mm dust-continuum images with and without the viscous accretion heating using the DSHARP opacity, and those without the viscous heating using the other three opacities. The comparison of the observed and model intensity profiles along the major axis with the DSHARP opacity is shown in Figure 7. Without internal heating, the peak intensity of the 1.3 mm dust-continuum emission is only about half of the observed intensity, regardless of the adopted opacity (Figures 6(c) and 7(b)). Incorporation of the viscous accretion heating raises the model intensities and reproduces the observed intensities (Figures 6(b) and 7(a)). This is the case for all the opacity tables.

We tried to reproduce the observed 1.3 mm intensity with the passive heating from the central protostar alone, adopting very high protostellar luminosities of $L_\star = 20\ L_\odot$ (Model 27 in Table 2), 26 $L_\odot$ (Model 49), and 52 $L_\odot$ (Model 60). We found that a central luminosity of 52 $L_\odot$ is required to reproduce the disk brightness. This luminosity, however, is one order of magnitude higher than the measured bolometric luminosity. Even if the uncertainty of the L_{bol} measurement is taken into account, this luminosity is still higher by a factor of about 7 than the highest possible value of L_{bol} (see Section 2.3). We also changed the disk mass and dust mass opacity and checked how the model 1.3 mm dust-continuum intensity changes with these parameters (see Table 2). Note that the disk mass and the dust mass opacity at the observed wavelength $\kappa_{1.3\mathrm{mm}}$ are degenerate in controlling the 1.3 mm intensity. We found that increasing M_d to 0.55 $M_\odot$ does not increase the model 1.3 mm intensity (Model 34). The different dust opacities seldom change the 1.3 mm intensity (Figure 6(c)). This indicates that the model 1.3 mm dust-continuum emission in the protostellar disk is optically thick. Thus, the only remaining way to raise the continuum intensity is to increase the dust temperature in the disk. Figures 8 and 9 show the temperature distributions of the models with and without viscous heating, which correspond to Figures 6(b) and (c) with the DSHARP opacity. It is clear that incorporation of the viscous accretion heating raises the midplane dust temperature in the inner $\lesssim$50 au, which enhances the dust emission intensities.

We conclude that the observed bright 1.3 mm intensity in the protostellar disk around IRS 7B-a cannot be reproduced with passive heating from the central protostar alone. In other words, the protostellar disk is self-luminous.

3.2. Asymmetry along the Minor Axis

Like the 1.3 mm dust-continuum intensity, the observed skewed distribution along the minor axis should be reproduced. Figure 10 shows model images (top) and intensity profiles along the disk minor axis (bottom) with different disk-flaring indices q. All other model parameters are set to the fiducial values. The flaring index q is defined in Equation (5). $q = 0$ indicates that the dust scale height increases linearly with r. $q = 0.25$ corresponds to a disk midplane temperature of $\propto r^{-0.5}$ and to a disk in the vertical hydro-equilibrium. In the case of $q = 0$, the model image exhibits a fairly symmetric feature (Figure 10(a)). The model intensity profile along the minor axis (red curve) shows little deviation from the symmetry. On the other hand, the observed intensity profile (black) shows a clear asymmetry, and there is a shallow shoulder to the southwest. When a steeper flaring index is adopted, the model images and intensity profiles are more strongly skewed along the minor axis. $q = 0.25$ reproduces the northeastern part of the observed intensity profile fairly well, while this index does not appear to be enough to reproduce the southwestern shoulder (Figure 10(b)). In the case of $q = 0.30$, the southwestern shoulder appears to be better reproduced, while there is a small deviation in the northeastern part (Figure 10(c)). When an even steeper flaring index is adopted (Figure 10(d)), the southwestern shoulder becomes too shallow.

We found that when archetypal disk models with a flaring of $\frac{h}{r} \propto r^{0.25}$ and a mass of $\lesssim 0.1\ M_\star$ are adopted, the model image exhibits a fairly symmetric intensity profile along the minor axis (models 12–18). It is necessary to raise the disk mass to $\sim 0.41\ M_\odot \approx 0.14\ M_\star$ to reproduce the observed asymmetry along the minor axis. On the other hand, a very high disk flaring $q \gtrsim 0.5$ is required to reproduce the asymmetry with a low disk mass (models 96–99). We found that either a higher flaring index or a higher disk mass is required and that the flaring index and the disk mass are degenerate, to produce the skewed emission distribution. As fiducial values, $q = 0.3$ and $M_{disk} = 0.41\ M_\odot$ are adopted.

Figure 11 presents a schematic figure to explain the cause of the asymmetry along the minor axis. We consider the lines of sight (LOSs) B and C offset from the LOS toward the disk center (LOS A). Even though the amount of the offset of these LOSs from the center are the same on the upper and lower sides in Figure 11, those on the lower side directly see the hot disk surface if the dust-continuum emission there is optically thick.

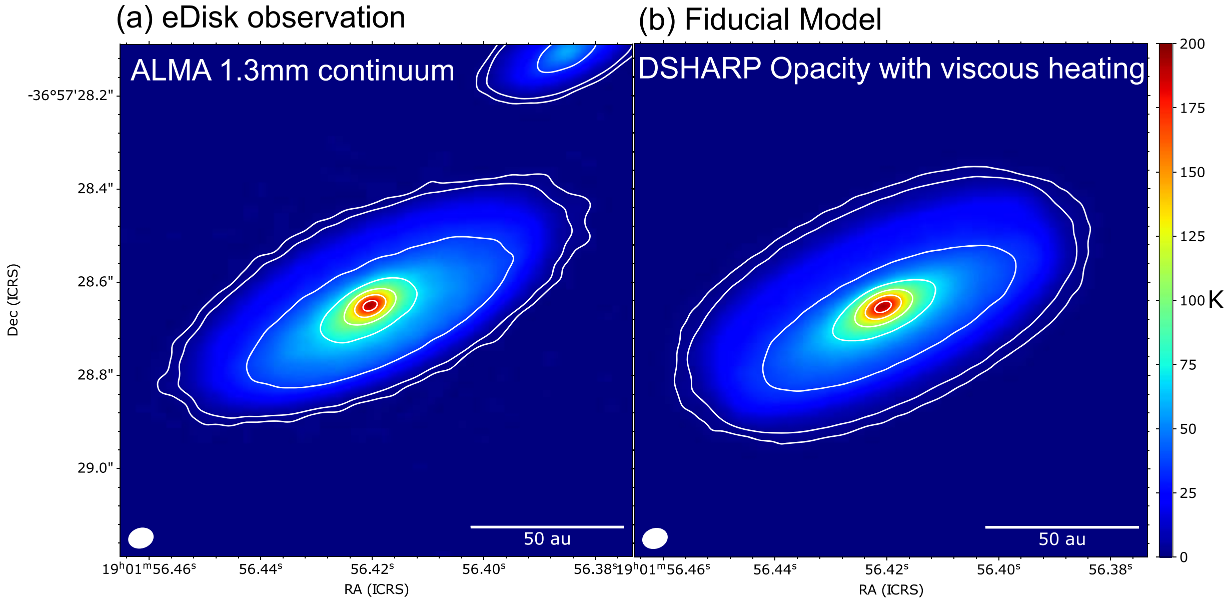

(c) Fiducial Models without viscous heating

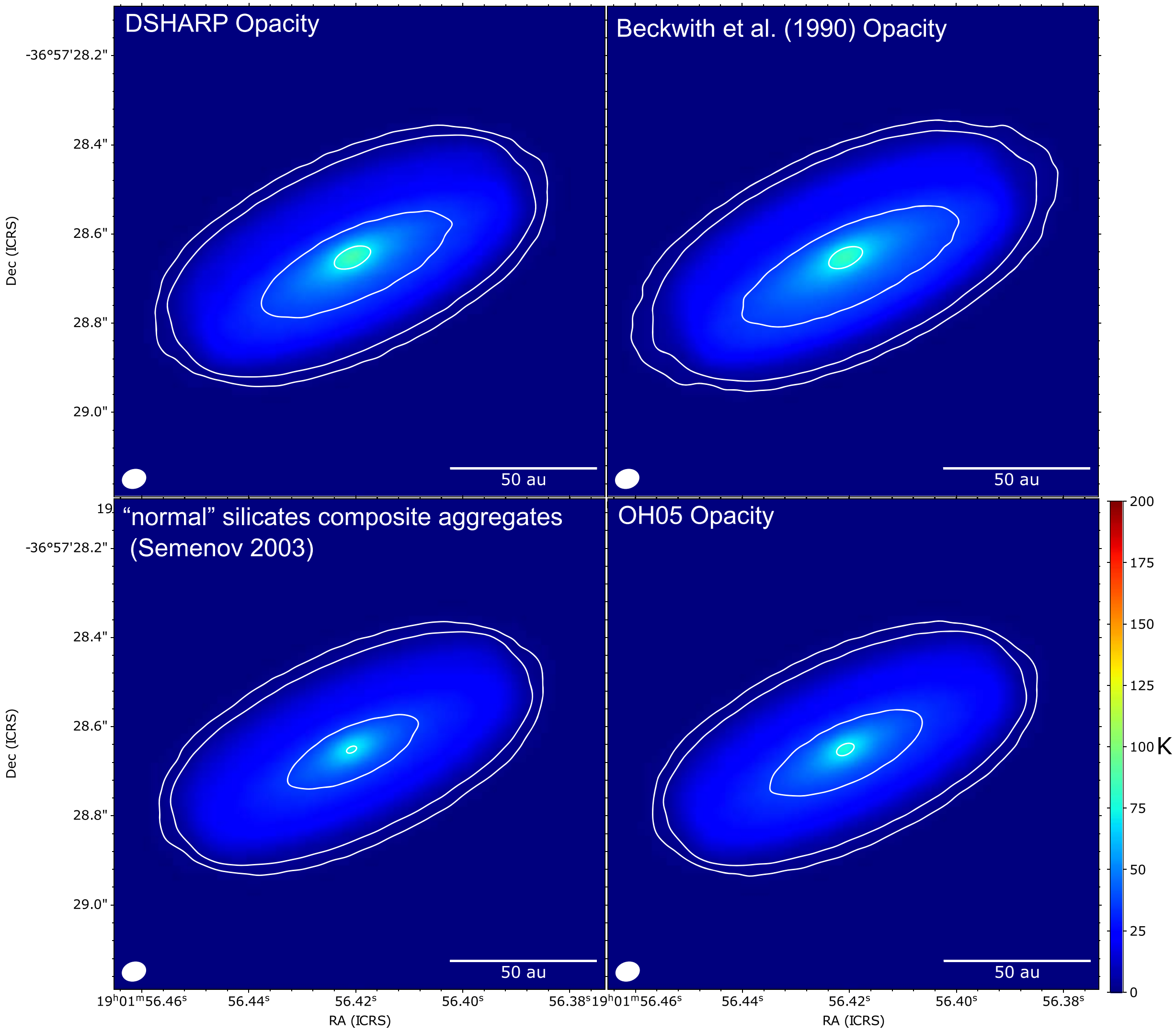

Figure 6. Comparison of the observed 1.3 mm dust-continuum image (a) to the model images with (b) or without viscous accretion heating (c). Contour levels are the same as those in Figure 1. The model image with the viscous accretion heating adopts the DSHARP opacity and a mass accretion rate of $\dot{M} = 1.4 \times 10^{-6}\,M_{\odot}\,\mathrm{yr}^{-1}$, while the model images without the heating adopts four different dust opacities as labeled. Panel (b) corresponds to model 61 in Table 2, and the four models in panel (c) correspond to models 66, 68, 69, and 70, respectively.

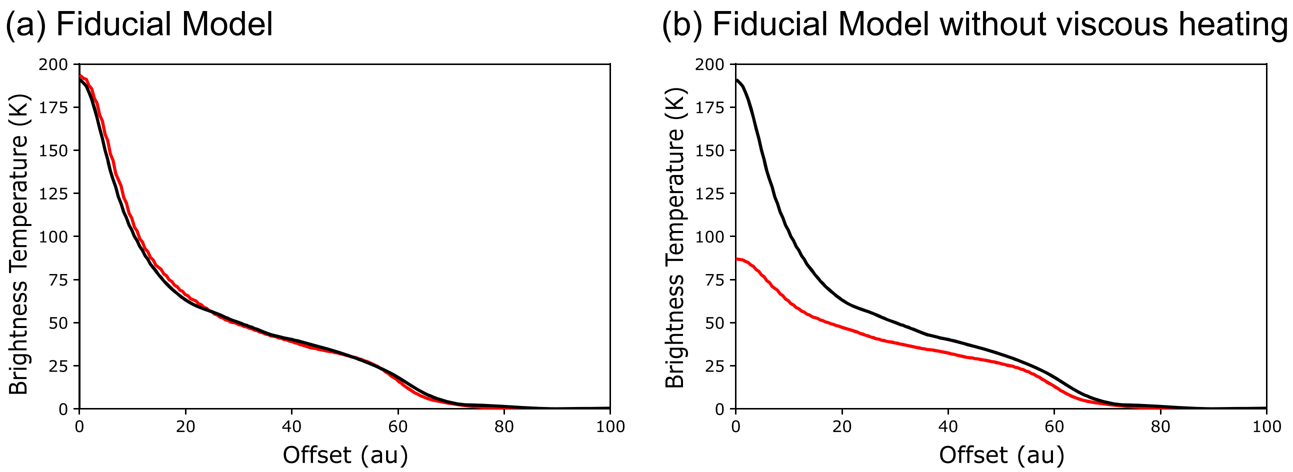

(a) Fiducial Model

(b) Fiducial Model without viscous heating

Figure 7. Comparison of the observed and model intensity profiles of the 1.3 mm dust-continuum emission. The black curves in panels (a) and (b) show the observed intensity profile averaged in the northwest and southeast directions along the major axis. The red curves in panels (a) and (b) present the model intensity profiles with (model 61 in Table 2) and without (model 66) viscous accretion heating, respectively.

(a) Temperature Distribution with viscous heating ($\dot{M} = 1.4 \times 10^{-6}\ M_\odot\ yr^{-1}$)

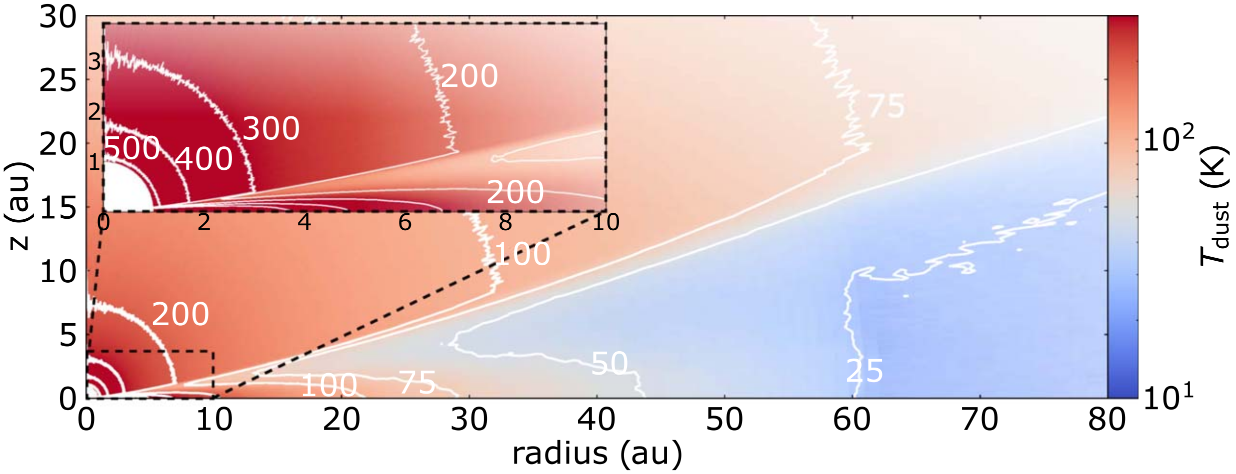

(b) Temperature Distribution without viscous heating

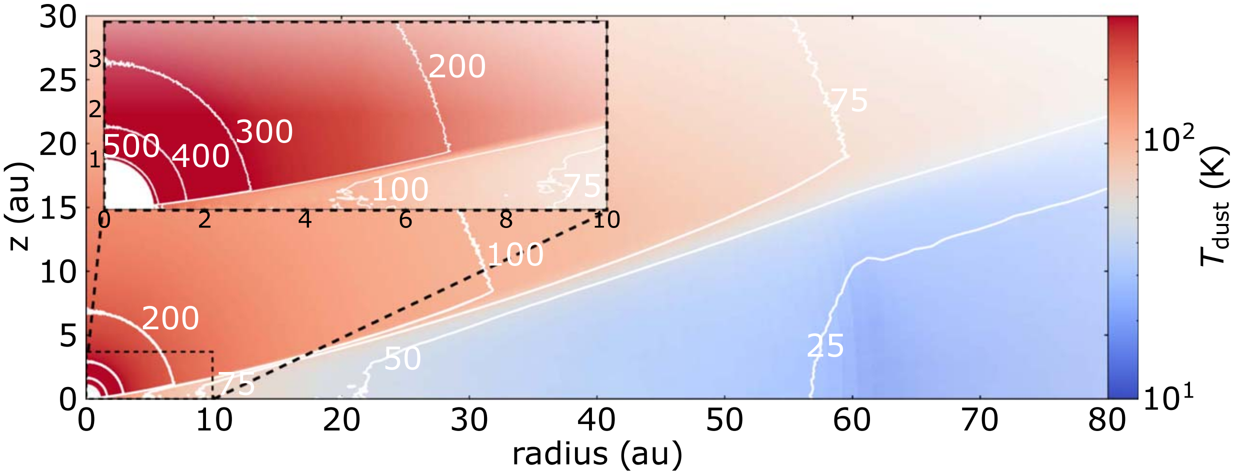

Figure 8. Distribution of the dust temperature in the disk region with (a; model 61 in Table 2) and without viscous accretion heating (b; model 66). The contour levels are 25, 50, 75, 100, 200, 300, 400, and 500 K.

On the other hand, on the upper side, the LOSs encounter the colder midplane regions. Thus, the overall emission distribution should be skewed to the lower side. If the LOSs are far from the disk center (LOS D), these portions become optically thin. Thus, at larger radii, the asymmetric distribution becomes less significant. These portions correspond to the elliptical

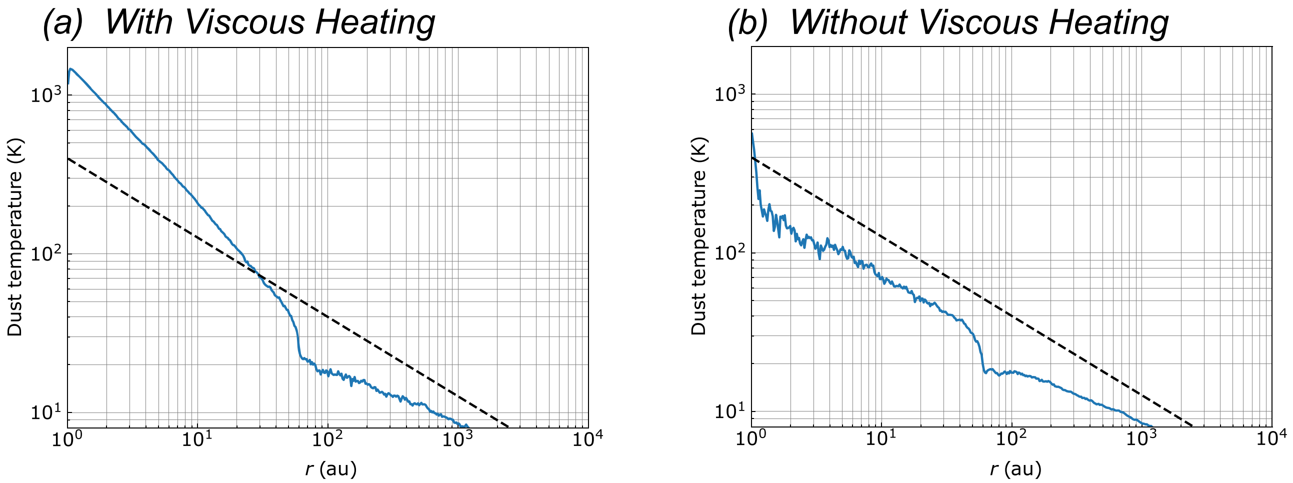

Figure 9. Radial temperature profiles (blue lines) in the disk midplane with (a; model 61 in Table 2) and without viscous accretion heating (b; model 66). The dashed lines show the temperature profile of 400 (K) $\times(r/1\ \text{au})^{-0.5}$.

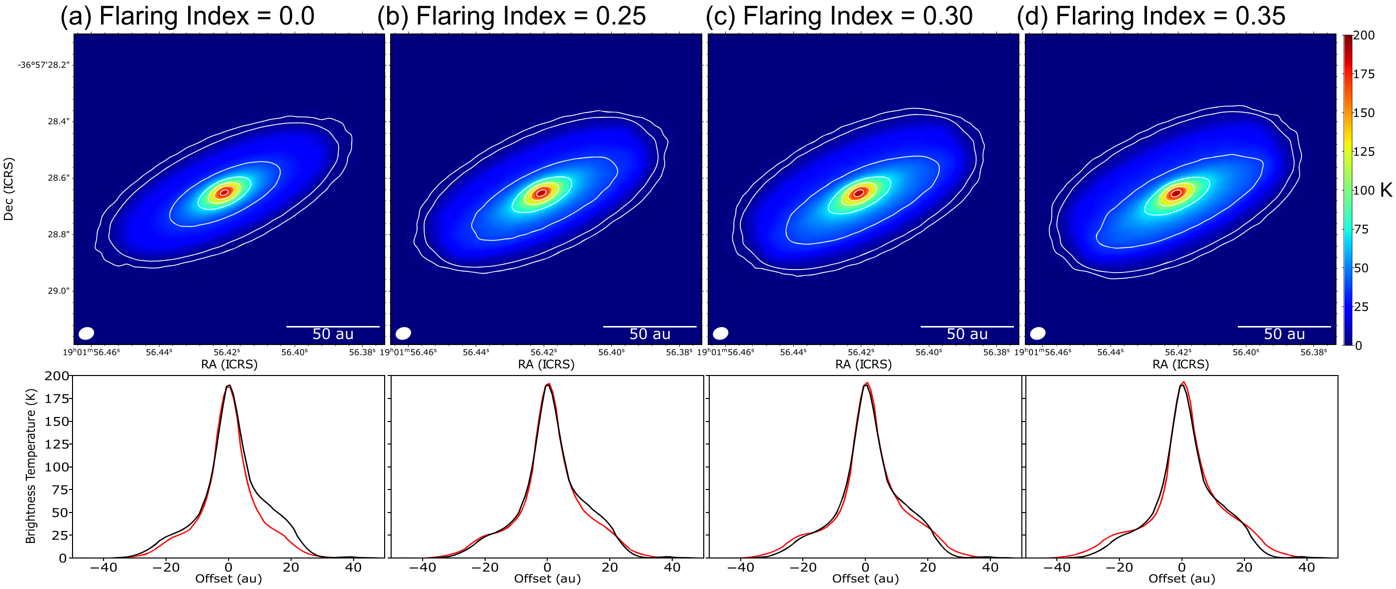

Figure 10. Upper panels: Model 1.3 mm dust-continuum images with different flaring indices of the dust distribution as labeled. The contour levels are the same as those in Figure 1. Lower panels: Relevant intensity distributions along the minor axis (red curves), to be compared to the observed intensity profile (black). Panels (a), (b), (c), and (d) correspond to models 4, 28, 61 (fiducial), and 85, respectively, in Table 2.

region as denoted by the dashed line in Figure 1. When the disk is more inclined or more flared, the LOS toward the disk center (LOS A) passes through a portion of the flared disk in the near side. The near-side portion of the flared disk affects the observed intensity at the central LOS, and the central position can be dimmer. The extreme case is the perfectly edge-on disk in HH 212 mms, which produces a dark lane at the disk midplane and a morphology that is shaped like a space hamburger (Lee et al. 2017).

Thus, both disk flaring and optically thickness of the dust emission are required to produce the skewed emission distribution. When the disk is perfectly geometrically thin or the dust emission is perfectly optically thin, the emission distribution should always be symmetric. The degeneracy between the flaring index and disk mass found by our modeling is naturally explained since more strongly flared disks require a lower optical depth, and less strongly flared disks require a greater optical depth. On the other hand, the disk stability with a given disk mass can be evaluated with the Toomre Q value as

$$Q = \frac{c_s \Omega_{\rm K}}{\pi G \Sigma}, \tag{21}$$

where the formulae of c_s, $\Omega_{\rm K}$, and Σ are given in Equations (3), (4), and (6), respectively. Note that the Q value depends on R. Adopting the fiducial disk mass of 0.41 $M_\odot$ and the dust temperature shown in Figure 9(a) to calculate c_s, the Toomre Q values are calculated to be ∼11.2, 2.2, and 1.0 at $R = 10$, 30, and 50 au, respectively. Thus, the inner region is gravitationally stable, but the outer region can be unstable. In combination with an appropriate value of the disk-flaring index of ∼0.3, the fiducial value of the disk mass is thus reasonable.

4. Modeling the $C^{18}O$ Image Cube

After reproducing the observed 1.3 mm dust-continuum image, we seek to reproduce the observed intensities and

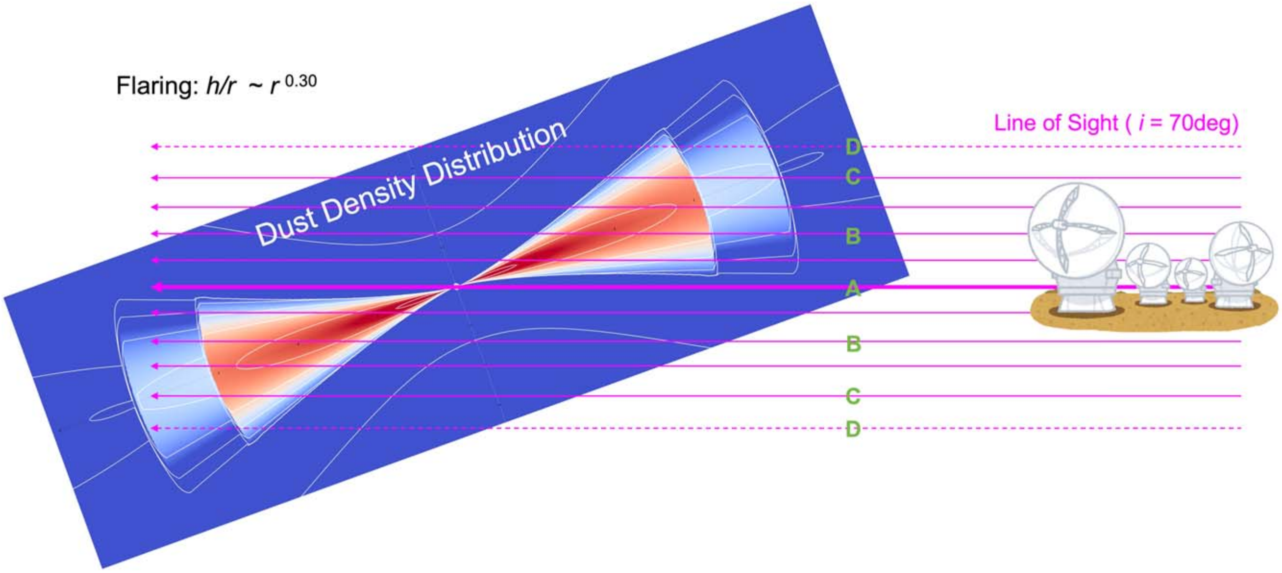

Figure 11. Schematic picture to interpret the skewed distribution of the 1.3 mm dust-continuum emission along the minor axis. The dust distribution in the model disk, inclined by 70° to the LOS of the observer, is shown. Lines of sight toward the center (A) and the offset positions (B, C, and D) are drawn. The contour levels and color scale are the same as in Figure 2(c).

spatial and velocity distributions of the $C^{18}O$ (2–1) emission next. The $C^{18}O$ (2–1) emission has been adopted as a good probe of protostellar disks and envelopes (e.g., Ohashi et al. 2014; Yen et al. 2014; Aso et al. 2015). The black contours and colors in Figure 12 show the observed velocity channel maps of the $C^{18}O$ (2–1) emission in IRS 7B-a (Ohashi et al. 2023). While the $C^{18}O$ emission exhibits a velocity gradient along the disk major axis and a signature of Keplerian rotation, the molecular emission is detected only in the outskirts of the dust disk (white contours in Figure 12). This is because the molecular emission is buried in the bright dust-continuum emission (see Section 5.2 for the mechanism of the absence of the molecular emission toward the dust-continuum emission).

In our modeling of the $C^{18}O$ emission, we first adopted the same radius of the gas disk as for the dust disk (e.g., $r_{\rm gas} = r_{\rm dust} = 62$ au in Model 74 and $r_{\rm gas} = r_{\rm dust} = 80$ au in Model 76; see Table 2). In these cases, however, the $C^{18}O$ emission is significantly suppressed, and the observed $C^{18}O$ emission cannot be reproduced. We found that a larger radius of the gas disk is required to reproduce the observed intensities as well as the spatial and velocity distributions of the $C^{18}O$ emission (fiducial Model 61). As both the $r_{\rm gas} = r_{\rm dust} = 62$ au and $r_{\rm gas} = r_{\rm dust} = 80$ au cases yield a significantly suppressed $C^{18}O$ emission, the difference of the gas and dust radii is unlikely to be due to the effect of the noise in the continuum data.

To ensure the difference of the gas and dust radii, the CASA observing simulator including the noise is applied to the calculated $C^{18}O$ model image cubes. Note that the signal-to-noise ratio of the continuum emission is higher than or comparable to that of the $C^{18}O$ emission in the $C^{18}O$ emission region (see Figure 12). Two model image cubes, one with $r_{\rm gas} = 80$ au and $r_{\rm dust} = 62$ au (fiducial) and the other with $r_{\rm gas} = r_{\rm dust} = 62$ au, are adopted for the CASA simulations. Note that these two models do not adopt the CASA task *ft* but *simobserve* to include the noise (Models 100 and 101, respectively). The model velocity channel maps of the $C^{18}O$ emission with the gas disk radius of 80 au (Model 100) are overlaid in Figure 12 (red contours). The overall locations of the $C^{18}O$ emission, shapes, and intensities are broadly reproduced with the model. Figure 13(a) compares the observed and model PV diagrams along the major axis of the dust disk. The observed emission location in the PV diagram is reproduced with the model. In contrast, the model with the gas radius identical to the dust radius (Model 101) cannot reproduce the observed intensities (Figure 13(b)). These results suggest that the radius of the gas disk is larger than that of the dust disk in IRS 7B-a.

5. Discussion

5.1. Self-luminous Protostellar Disks

Our modeling and parameter search found that models of dusty disks that are only passively heated by the central protostar cannot reproduce the observed bright 1.3 mm dust-continuum intensities. The observed peak brightness temperature is as high as ∼195 K. To reproduce this high dust brightness temperature, internal heating by the viscous accretion, along with optically thick dust emission, is incorporated. Then, the observed brightness temperature in the disk can be reproduced with a typical mass accretion rate of about a few $\times 10^{-6}\ M_\odot\ {\rm yr}^{-1}$. In other words, the inner part of the IRS 7B-a disk is self-luminous, and most of the heating comes from the release of gravitational energy as the material in the disk gradually spirals inward as it loses angular momentum.

The high peak brightness temperature of the 1.3 mm dust-continuum emission in IRS 7B-a is not unique, but is also seen in several other eDisk targets, such as IRAS 04166 + 2706 (133 K), BHR 71 IRS1 (170 K), Oph IRS 63 (170 K), R CrA IRAS 32A (153 K), and TMC-1A (187 K) (Ohashi et al. 2023). While a modeling effort tailored for these targets is required, these high brightness temperatures likely suggest that these protostellar disks are also self-luminous. In contrast, none of the 20 sources in the DSHARP sample shows a peak brightness temperature of the 1.3 mm dust-continuum emission higher than 150 K, and most sources show peak brightness temperatures lower than ∼60 K (Andrews et al. 2018). The

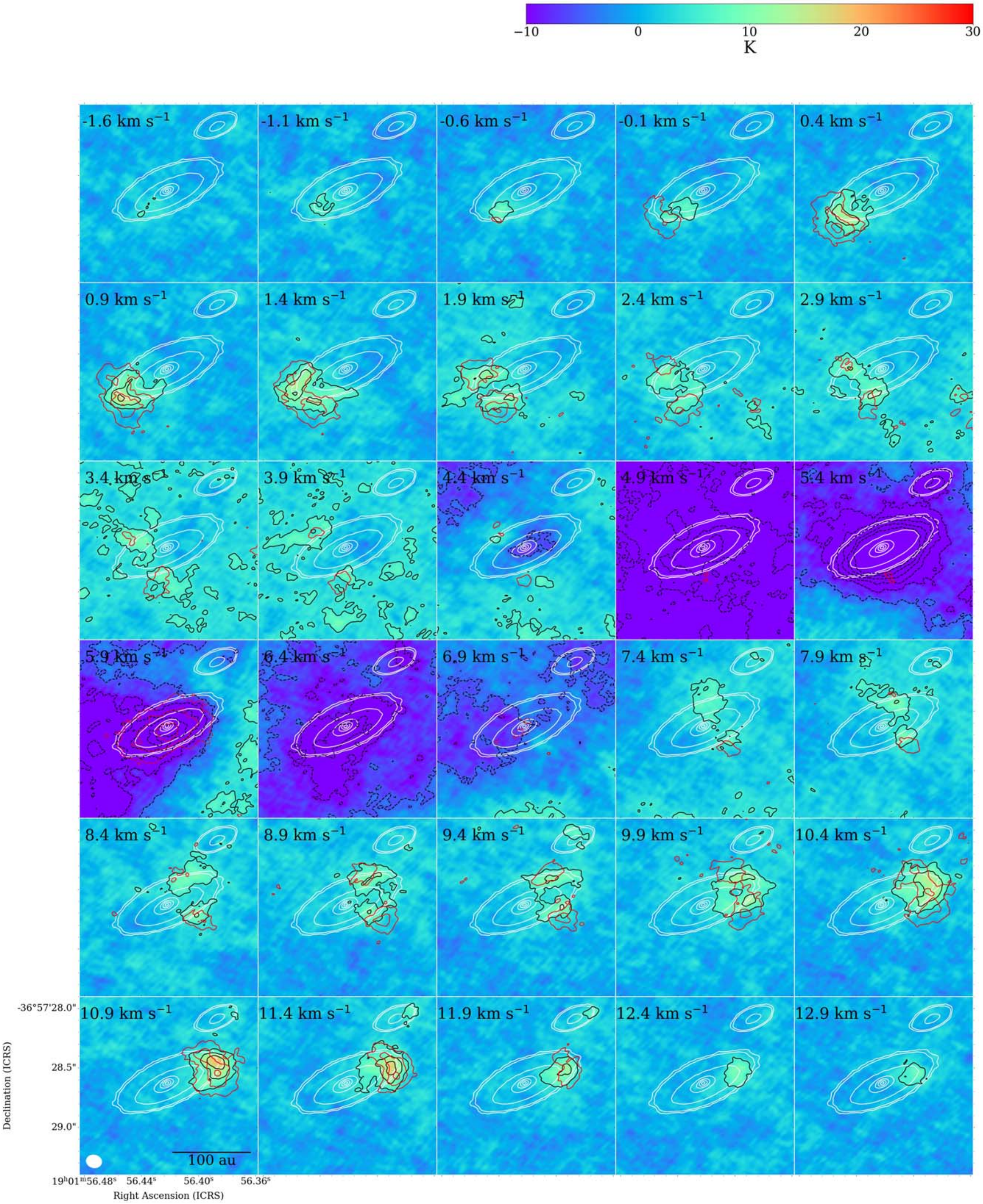

Figure 12. Comparison of the observed (black contours and colors) and model C^{18}O (2–1) velocity channel maps (red) in IRS 7B-a (Model 61 in Table 2). The contour levels of the C^{18}O emission start from -18σ in steps of 3σ ($1\sigma = 1.72$ K). The white contours show the map of the observed 1.3 mm dust-continuum emission, where the contour levels are same as in Figure 1.

peak 1.3 mm brightness temperatures of edge-on Class II disks are even lower (5–10 K; Villenave et al. 2020). These results suggest a systematic difference of the physical conditions between the protostellar and protoplanetary disks.

Alarcón et al. (2024) constructed detailed models of the dust disk around V883 Ori, a Class I FU-Ori object, which has been studied as an intriguing astrochemical laboratory (van 't Hoff et al. 2018; Tobin et al. 2023). Their model also demonstrates

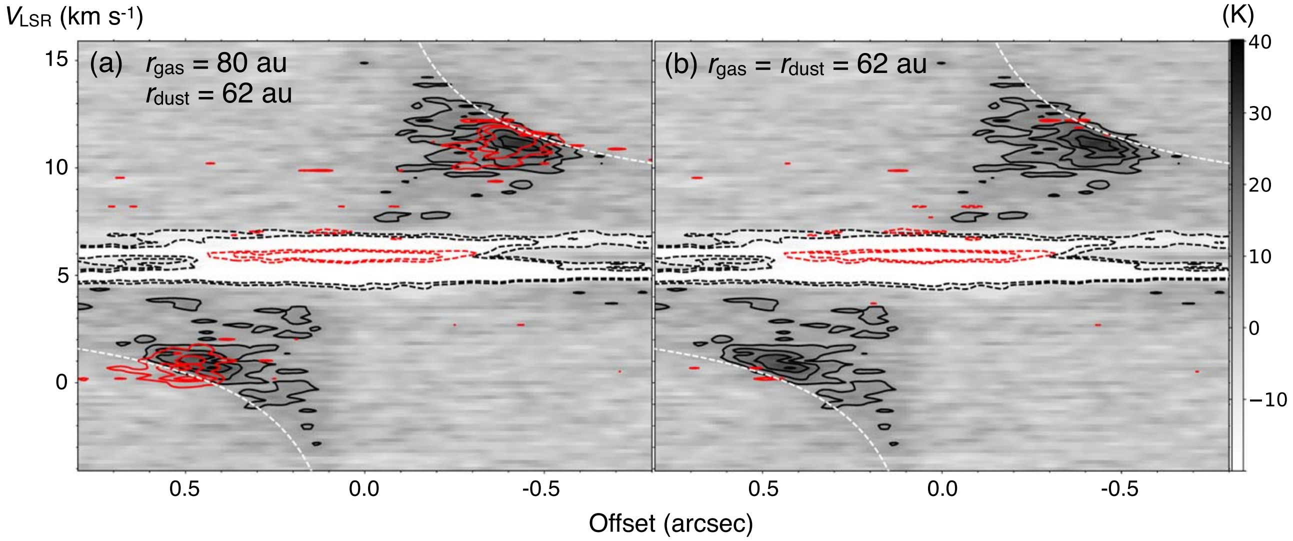

Figure 13. Comparison between the observed (black contours and grayscale) and model PV diagrams (red contours) of the $C^{18}O$ (2–1) emission along the major axis (P.A. $= 115°$). Panel (a) shows the model PV diagram with a dust radius of 62 au and a gas radius of 80 au including the noise (Model 100 in Table 2), while panel (b) with the gas and dust radius of 62 au including the noise (Model 101). The contour levels are -5σ, -3σ, 3σ, 5σ, 7σ, 9σ, and 11σ ($1\sigma = 2.98$ K). The dashed white curves denote the Keplerian rotation curve with a central protostellar mass of 2.9 $M_\odot$ and a disk inclination angle $i = 70°$.

that viscous accretion heating is required to reproduce the observed high (~500 K) brightness temperature of the 1.3 mm dust-continuum emission. The presence of viscous accretion heating in protostellar disks has also been suggested in other variable sources (Contreras Peña et al. 2020; Yoon et al. 2021) and in the massive protostar GGD 27-MM1 (Añez-López et al. 2020). While IRS 7B appears to be more quiescent than V883 Ori, our modeling also proves that even in the quiescent phase, viscous accretion heating is required to reproduce the dust brightness.

5.2. Coupling between Dust and Molecular Line Emission

In this subsection, we argue that the observed high brightness temperatures of the dust emission affect the interpretation of the molecular line images. We here consider two simple cases (see Bosman et al. 2021). One case is that the dust and gas are located in separate layers (e.g., disk and envelope) and that the optically thick dust emission resides behind the foreground molecular emission. In this case, the observed brightness temperature of the molecular line ($\equiv T_B^{\rm mol}$) is expressed as

$$T_B^{\rm mol} = (J_\nu(T_{\rm ex}) - J_\nu(T_{\rm dust}))(1 - \exp(-\tau_{\nu,{\rm gas}})), \tag{22}$$

where

$$J_\nu(T) = \frac{\frac{h_P\nu}{k_{\rm B}}}{1 - \exp\left(\frac{h_P\nu}{k_{\rm B}T}\right)}. \tag{23}$$

In the above expressions, ν is the line frequency, h_P is Planck constant, $T_{\rm ex}$ is the excitation temperature of the molecular line, and $T_{\rm dust}$ is the dust temperature. $\tau_{\nu,{\rm gas}}$ is the optical depth of the molecular line. When $T_{\rm ex}$ is close to $T_{\rm dust}$, $T_B^{\rm mol}$ is close to zero, regardless of the value of $\tau_{\nu,{\rm gas}}$ or the molecular column density. When $T_{\rm ex}$ is lower than $T_{\rm dust}$, the line is in absorption.

The other case is that both dust and gas are in the same space with the same volume. $T_B^{\rm mol}$ is expressed as

$$\begin{aligned} T_B^{\rm mol} &= J_\nu(T)(1 - \exp(-(\tau_{\nu,{\rm dust}} + \tau_{\nu,{\rm gas}})) \\ &\quad - J_\nu(T)(1 - \exp(-\tau_{\nu,{\rm dust}})) \\ &= J_\nu(T)\exp(-\tau_{\nu,{\rm dust}})(1 - \exp(-\tau_{\nu,{\rm gas}})). \end{aligned} \tag{24}$$

Here, we assume $T_{\rm ex}$=$T_{\rm dust}$=T. In this case, when $\tau_{\nu,{\rm dust}} \gg \tau_{\nu,{\rm gas}}$, $T_B^{\rm mol}$ is close to zero. Note that the absolute value of the dust optical depth does not matter. In the case of $\tau_{\nu,{\rm dust}} \gg \tau_{\nu,{\rm gas}}$, $T_B^{\rm mol}$ is always very low even when $\tau_{\nu,{\rm dust}} < 1$.

A depression or even absorption of the molecular line emission toward the continuum emission is commonly seen in ALMA observations of protostellar sources, including our eDisk observations (Lin et al. 2023b; Hoff et al. 2023). These phenomena are often referred to as continuum oversubtraction. From the considerations above, a possible reason for the absence of molecular line emission toward the continuum emission is either line excitation temperatures close to or lower than the dust temperatures, a dust optical depth higher than the line optical depth, or a combination of the two. A high dust temperature and a high dust optical depth both produce high observed dust brightness temperatures. In the case of protostellar sources, molecular emission originates not only from the protostellar disk, but also from the protostellar envelope. At lower velocities, the molecular emission from the disk is blended with that from the colder envelope. This envelope blending induces suppression or absorption of the molecular line toward the bright dust disk. The observed velocity channel maps indeed show that around the systemic velocity ($V_{\rm LSR} = 4.90$–6.40 km s^{-1}), no line emission is observed, but a strong absorption feature (Figure 12). The $C^{18}O$ model does not predict any emission in this velocity range. While the line width of the absorption feature is narrower, the $C^{18}O$ model also reproduces the absorption feature at $V_{\rm LSR} = 5.9$ km s^{-1}, as shown with the dashed red contours in Figure 12.

To trace the gas structures, kinematics, and chemistry in the inner parts of dusty disks, molecular lines that are optically thicker than the dust emission are required. On the other hand, when the optical depth of that molecular line is too high, the molecular line cannot trace the internal disk structures (Liu et al. 2018). In the case of embedded sources, optically thick molecular lines only trace the cold outer envelopes, which results in absorption against the bright continuum emission that originates from the disk. It is not straightforward to identify appropriate molecular tracers for protostellar disks. Different degrees of the missing flux between the continuum and line images in interferometric observations also complicate the interpretation of the observed images. When the original line + continuum image is totally uniform because of the optically thick line emission, the line + continuum image after the interferometric observations is severely suppressed. After the continuum subtraction, the line-only image shows a negative signal at the continuum position.

It is important to recall that our model assumes a constant $C^{18}O$ abundance and gas-to-dust mass ratio in the disk and envelope, except for the outer dust-free region in the disk (Figure 2). Our modeling demonstrates that even in this case, the $C^{18}O$ emission is suppressed in the disk. The observed image could be misunderstood as CO depletion in the disk. The same warning applies to the analysis of other lines. Detailed radiative transfer modeling coupled with the interferometric observing simulations is required to correctly interpret the interferometric images and to quantitatively study the physical and chemical conditions of protostellar disks.

5.3. Dust Distribution in the Protostellar Disk

Our modeling also found that the observed skewness of the 1.3 mm dust-continuum emission along the disk minor axis can be reproduced with the flared disk model and that the dust emission is optically thick. The dust in the protostellar disk has yet to settle. These asymmetric distributions of the 1.3 mm dust-continuum emission along the disk minor axes are also observed in other eDisk targets, including CB 68 (Kido et al. 2023), L1527 IRS (Hoff et al. 2023), IRAS 04302 + 2247 (Lin et al. 2023b), and GSS30 IRS 3 (A. Santamaría-Miranda et al. 2023, in preparation), as well as the space hamburger in HH212 mms (Lee et al. 2017). These results suggest that at least in several of the protostellar disks, the dust vertical distributions are flared (Ohashi et al. 2023).

The above result is in sharp contrast to the observed geometrically thin dust distributions in protoplanetary disks around Class II sources. Concentric ring/gap features are commonly seen in such Class II disks. When the dust distributions are flared vertically and the disk rotational axes are inclined with respect to the LOS, these ring/gap features can easily be hidden by the geometrical effect. Thus, the dust is already settled in these more evolved disks (Pinte et al. 2016). The 1.3 mm dust-continuum images of highly inclined ($i \gtrsim 70°$) Class II disks also show ring/gap features, which strongly implies that the dust distribution is geometrically thin (Villenave et al. 2020, 2022). Two of the eDisk targets, the most evolved sources L1489 IRS and Oph IRS63, show signatures of concentric rings/gaps in the disks (Flores et al. 2023; Ohashi et al. 2023; Yamato et al. 2023). These disks do not show an asymmetry along the disk minor axes. Dust settling and the formation of ring/gap features in the disks are thought to likely proceed between the Class I to Class II stages, as also discussed in Ohashi et al. (2023).

On the other hand, our combined dust continuum and $C^{18}O$ modeling also revealed that the radius of the gas disk (∼80 au) should be larger than that of the dust disk (∼60 au) around the Class I protostar IRS 7B-a. In more evolved protoplanetary disks around Class II sources, the observationally measured radii of CO disks (e.g., curves of growth) are systematically larger than the corresponding dust radii, and the gas radii are 2–2.5 times larger than the dust radii (Ansdell et al. 2018; Andrews 2020). The effect of the optical depth and radial variation of the dust κ, however, complicates the interpretation of the apparent discrepancy between the gas and dust radii (Hughes et al. 2008). Trapman et al. (2019) suggested that gas radii larger by a factor of 4 are required to unambiguously prove the radial drift of dust. On the other hand, simultaneous radiative transfer modeling of gas and dust disks showed that the same gas and dust radii with the constant gas-to-dust ratio cannot reproduce the CO and the dust intensity profiles and the difference between them (Panić et al. 2009; Andrews et al. 2012; Ansdell et al. 2018; Facchini et al. 2019). These results imply the presence of dust radial drift in the Class II stage. In the case of the Class I protostar IRS 7B, we make use of the simple observational results that the molecular line is severely suppressed due to the strong dust emission in the dust disk region, and that the gas emission is only visible in the outskirts of the dust disk. To reproduce these observational images, a gas disk radius larger than the dust radius should be incorporated. This implies that dust grains may have migrated radially inward with respect to the molecular gas in the Class I disk, even though they are not yet settled onto the disk midplane.

The above conclusion may seem surprising at first sight. In the simplest case of a smooth laminar disk, the timescale for radial migration of the dust relative to the gas,

$$t_{\rm rad} \equiv \frac{R}{|v_{r,d} - v_{r,\rm gas}|} \approx \frac{1}{\eta\ \tau_s\ \Omega_K}, \tag{25}$$

is much longer than the timescale for the dust to settle vertically,

$$t_z \equiv \frac{z}{|v_{z,d}|} \approx \frac{1}{\tau_s\ \Omega_K} \tag{26}$$

in the small particle limit (with the dimensionless Stokes number $\tau_s \ll 1$; see Sections 7.1 and 7.2 of the review article by Armitage 2017), where R is the cylindrical radius, $v_{r,d}$ and $v_{r,\rm gas}$ are the radial velocity of the dust and gas, respectively, Ω_K is the local Keplerian frequency, z is the vertical distance from the midplane, $v_{z,d}$ is the dust settling terminal speed, and $\eta \propto (h/R)^2 \ll 1$ measures the fractional deviation of the gas rotation speed from the local Keplerian value. A potential solution to this apparent contradiction is that the dust is prevented from settling by turbulence in the disk, which may also be required to drive the relatively high mass accretion rate inferred from the dust-continuum modeling. The nature of the turbulence and how it may affect the radial dust migration remains unclear and deserves further investigation. In the circumternary dust ring around the GG Tau system, Tang et al. (2023) proposed that the angular difference of the polarization direction from the tangent of the ring could be due to the radial flow of the dust grains. The radial drift velocity estimated from the angle difference, however, is about three times faster than the theoretical prediction using the same formula by Armitage (2017).

6. Summary

We have constructed a physical model that reproduces the 1.3 mm dust-continuum emission and the C^{18}O (2–1) emission toward the Class I protostar R CrA IRS 7B-a, which was observed with our ALMA Large Program, eDisk. The gas and dust density distributions are given, and thermal Monte Carlo simulations are performed to calculate the spatial distribution of the dust temperature with RADMC-3D. From the spatial distributions of gas and dust as well as the calculated temperature distribution, the images of the 1.3 mm dust-continuum emission and C^{18}O (2–1) emission are made with RADMC-3D, followed by the observing simulations. A number of such images were created to search by eye for the model parameters that decently reproduce the intensities and the spatial and velocity distributions of the observed emissions. Our modeling effort has found the following insights into the physical properties of the protostellar disk.

1. Dust disk models that are passively heated by the central protostar alone cannot reproduce the observed bright intensity of the 1.3 mm continuum emission, regardless of the adopted dust mass opacity table and disk mass. The 1.3 mm dust-continuum emission in the disk is optically thick, and a change of $\kappa_{1.3\mathrm{mm}}$ or disk mass does not increase the 1.3 mm intensity significantly. The 1.3 mm intensity in these models is a factor $\gtrsim$2 lower than the observed intensity. We found that the inclusion of the viscous accretion heating in the disk with a mass accretion rate of $\dot{M}\sim 10^{-6}\ M_{\odot}\ \mathrm{yr}^{-1}$ can reproduce the observed 1.3 mm intensities. Several other eDisk targets also exhibit similar high brightness temperatures of the 1.3 mm dust-continuum emission originating from the disk. These results suggest that the protostellar disks are self-luminous. In contrast, disks around Class II sources do not show high dust intensities like htis, suggesting a difference in the physical conditions between the protostellar and Class II disks.
2. The observed asymmetry of the 1.3 mm dust-continuum image along the minor axis is reproduced with a flared dust disk model, where the flaring power-law index $q\sim 0.3$ is defined by $\frac{h}{r}\sim r^q$ and the disk mass is ~14% of the central protostellar mass. The flaring index and disk mass are degenerate in reproducing the observed skewed intensity profile along the disk minor axis. This is because the $\tau = 1$ disk surface is determined by the dust mass distribution, which in turn is set by the total dust mass and flaring parameter. Similar asymmetric structures of the dust emission along the disk minor axes are seen toward several other eDisk protostellar disks, suggesting that the dust in these protostellar disks yet has to settle to the midplane. This is different from the geometrically thin dust distribution in the disks around Class II sources associated with ring/gap features. These results suggest that dust settling and formation of ring/gap features in the disks proceed between the Class I and Class II stages.
3. To reproduce the observed distribution of the C^{18}O emission, the radius of the gas disk should be ~80 au, i.e., larger than that of the dust disk (~60 au). In models in which the gas disk radius is identical to the dust disk radius, the molecular emission is severely suppressed because of the obscuration by the high brightness and opacity of the dust emission.
4. Our radiative transfer model, combined with the observing simulations, reproduces the observed depression of the C^{18}O emission toward the continuum emission. Around the systemic velocity, the observed absorption of the C^{18}O line is also reproduced with our model. The absorption feature should originate from the higher background dust brightness temperature than the line excitation temperature. The depression of the molecular emission is also caused by the higher dust optical depth than the line optical depth. Note that gas components are present throughout the disk, with a constant C^{18}O abundance, in our models. While the apparent depressions of the molecular emission in the disks observed with ALMA are often interpreted as a real depletion of the molecule, they could be caused by radiative transfer effects, which are further enhanced by interferometric filtering. Detailed radiative transfer modeling and interferometric observing simulations are required to correctly interpret interferometric images.

Acknowledgments

We would like to thank all the ALMA staff supporting this work. S.T. is supported by JSPS KAKENHI grant Nos. JP21H00048 and JP21H04495 and by NAOJ ALMA Scientific Research grant No. 2022-20A. K.S. is supported by JSPS KAKENHI grant No. JP21H04495. N.O. acknowledges support from National Science and Technology Council (NSTC) in Taiwan through grants NSTC 109-2112-M-001-051 and 110-2112-M-001-031. J.J.T. acknowledges support from NASA RP 80NSSC22K1159. J.K.J., R.S., and S.G. acknowledge support from the Independent Research Fund Denmark (grant No. 0135-00123B). Y.A. acknowledges support by NAOJ ALMA Scientific Research Grant code 2019-13B, Grant-in-Aid for Scientific Research (S) JP18H05222, and Grant-in-Aid for Transformative Research Areas (A) JP20H05844 and JP20H05847. P.M.K. acknowledges support from NSTC 108-2112-M-001-012, NSTC 109-2112-M-001-022, and NSTC 110-2112-M-001-057. W.K. was supported by the National Research Foundation of Korea (NRF) grant funded by the Korea government (MSIT; NRF-2021R1F1A1061794). C.W.L. is supported by the Basic Science Research Program through the NRF funded by the Ministry of Education, Science and Technology (NRF-2019R1A2C1010851) and by the Korea Astronomy and Space Science Institute grant funded by the Korea government (MSIT; project No. 2024-1-841-00). J.-E.L. is supported by the NRF grant funded by the Korean government (MSIT; grant No. 2021R1A2C1011718). Z.-Y.L. is supported in part by NASA NSSC20K0533 and NSF AST-2307199 and AST-1910106. Z.-Y.D.L. acknowledges support from the Jefferson Scholars Foundation, the NRAO ALMA Student Observing Support (SOS) SOSPA8-003, the Achievements Rewards for College Scientists (ARCS) Foundation Washington Chapter, the Virginia Space Grant Consortium (VSGC), and UVA research computing (RIVANNA). L.W.L. acknowledges support from NSF AST-2108794. S.M. is supported by JSPS KAKENHI grant Nos. JP21J00086 and JP22K14081. P.D.S. acknowledges support from NSF AST-2001830 and NSF AST-

2107784. K.T. is supported by JSPS KAKENHI grant Nos. JP21H04487, JP22KK0043, and JP21H04495. J.P.W. acknowledges support from NSF AST-2107841. Y.Y. acknowledges support by JSPS KAKENHI Grant No. JP23KJ0636 and the International Graduate Program for Excellence in Earth-Space Science (IGPEES), World-leading Innovative Graduate Study (WINGS) Program of the University of Tokyo. H.-W.Y. acknowledges support from the NSTC in Taiwan through grant NSTC 110-2628-M-001-003-MY3 and from the Academia Sinica Career Development Award (AS-CDA-111-M03). This paper makes use of the following ALMA data: ADS/JAO.ALMA #2019.1.00261.L and 2019.A.00034.S. ALMA is a partnership of ESO (representing its member states), NSF (USA), and NINS (Japan), together with NRC (Canada), NSTC and ASIAA (Taiwan), and KASI (Republic of Korea), in cooperation with the Republic of Chile. The Joint ALMA Observatory is operated by ESO, AUI/NRAO, and NAOJ. The National Radio Astronomy Observatory is a facility of the National Science Foundation operated under cooperative agreement by Associated Universities, Inc.

Facility: ALMA

Software: CASA (McMullin et al. 2007), matplotlib (Hunter 2007), RADMC-3D (Dullemond 2012), bettermoments (Teague & Foreman-Mackey 2018; Teague 2019), PVextractor (Ginsburg et al. 2016), APLpy (Robitaille & Bressert 2012; Robitaille 2019), SLAM (Aso & Sai 2023), astropy (Astropy Collaboration et al. 2022).

Appendix
Searched Model Parameters

Table 2 lists all the sets of the calculated model parameters, sorted by the disk-flaring index q and then the disk mass M_d, except for Models 100–102, which adopt *simobserve* instead of *ft*. Note that we did not attempt to cover the complete parameter space, but tried to approach to the model images that reproduce the observed images.

Table 2
Parameter Search for the IRS 7B-a Modeling

Model	Grid (r, θ, ϕ)	Flaring Index, q	M_d ($M_\odot$)	$r_{\rm dust}$ (au)	$r_{\rm gas}$ (au)	Mass Accretion Rate $\dot{M}$ ($\times 10^{-6}$ $M_\odot$ yr^{-1})	Dust Opacity	Disk Inclination (deg)	Stellar Luminosity ($L_\odot$)
1	(512, 512, 1)	0.00	0.39	60	80	0.0	Beckwith	−70	5.2
2	(512, 512, 1)	0.00	0.39	60	80	1.9	Beckwith	−70	5.2
3	(512, 512, 1)	0.00	0.39	60	80	1.4	Beckwith	−70	5.2
4	(512, 512, 1)	0.00	0.41	62	80	1.4	DSHARP	−70	5.2
5	(512, 512, 1)	0.00	0.55	62	80	1.4	DSHARP	−70	5.2
6	(512, 512, 1)	0.20	0.39	60	80	1.4	Beckwith	−70	5.2
7	(256, 256, 1)	0.20	0.39	60	80	1.9	Beckwith	−70	5.2
8	(512, 512, 1)	0.20	0.41	62	80	1.4	DSHARP	−70	5.2
9	(256, 256, 1)	0.20	0.45	60	80	1.9	Beckwith	−70	5.2
10	(512, 512, 1)	0.20	0.55	62	80	1.4	DSHARP	−70	5.2
11	(512, 512, 1)	0.20	0.68	62	80	1.4	DSHARP	−70	5.2
12	(256, 256, 1)	0.25	0.03	60	80	5.1	Beckwith	−70	5.2
13	(256, 256, 1)	0.25	0.06	60	80	2.9	Beckwith	−70	5.2
14	(256, 256, 1)	0.25	0.13	60	80	2.3	Beckwith	−70	5.2
15	(256, 256, 1)	0.25	0.19	60	80	2.0	Beckwith	−70	5.2
16	(512, 512, 1)	0.25	0.20	62	80	1.4	DSHARP	−70	5.2
17	(256, 256, 1)	0.25	0.26	60	80	1.9	Beckwith	−70	5.2
18	(512, 512, 1)	0.25	0.27	62	80	1.4	DSHARP	−70	5.2
19	(256, 256, 1)	0.25	0.32	60	80	1.9	Beckwith	−70	5.2
20	(512, 512, 1)	0.25	0.39	60	80	1.4	Beckwith	−70	5.2
21	(512, 512, 1)	0.25	0.39	60	80	1.9	Beckwith	−70	5.2
22	(512, 512, 1)	0.25	0.39	60	80	1.9	DSHARP	−70	5.2
23	(512, 512, 1)	0.25	0.39	60	80	1.9	Beckwith	−70	20.0
24	(512, 512, 1)	0.25	0.39	60	80	1.9	Beckwith	−72	20.0
25	(512, 512, 1)	0.25	0.39	60	80	1.9	Beckwith	−74	20.0
26	(512, 512, 1)	0.25	0.39	60	80	0.0	Beckwith	−70	5.2
27	(512, 512, 1)	0.25	0.39	60	80	0.0	Beckwith	−70	20.0
28	(512, 512, 1)	0.25	0.41	62	80	1.4	DSHARP	−70	5.2
29	(512, 512, 1)	0.25	0.45	60	80	1.7	Beckwith	−70	5.2
30	(512, 512, 1)	0.25	0.45	60	80	1.7	Beckwith	−72	5.2
31	(512, 512, 1)	0.25	0.45	60	80	1.7	Beckwith	−75	5.2
32	(256, 256, 1)	0.25	0.45	60	80	1.9	Beckwith	−70	5.2
33	(512, 512, 1)	0.25	0.55	62	80	1.4	DSHARP	−70	5.2
34	(512, 512, 1)	0.25	0.55	62	80	0.0	DSHARP	−70	5.2
35	(512, 512, 1)	0.25	0.68	62	80	1.4	DSHARP	−70	5.2
36	(256, 256, 1)	0.30	0.06	60	80	2.9	Beckwith	−70	5.2
37	(256, 256, 1)	0.30	0.13	60	80	2.3	Beckwith	−70	5.2
38	(256, 256, 1)	0.30	0.19	60	80	2.0	Beckwith	−70	5.2
39	(512, 512, 1)	0.30	0.20	62	80	1.4	DSHARP	−70	5.2
40	(256, 256, 1)	0.30	0.26	60	80	2.0	Beckwith	−70	5.2
41	(512, 512, 1)	0.30	0.27	62	80	1.4	DSHARP	−70	5.2
42	(512, 512, 1)	0.30	0.32	60	80	1.9	Beckwith	−68	5.2
43	(512, 512, 1)	0.30	0.32	60	80	1.9	Beckwith	−70	5.2
44	(512, 512, 1)	0.30	0.32	60	80	1.9	Beckwith	−72	5.2
45	(512, 512, 1)	0.30	0.39	60	80	1.4	Beckwith	−70	5.2
46	(512, 512, 1)	0.30	0.39	60	80	1.3	Beckwith	−70	5.2
47	(512, 512, 1)	0.30	0.39	60	80	1.2	Beckwith	−70	5.2

Table 2
(Continued)

Model	Grid (r, θ, ϕ)	Flaring Index, q	$M_{\rm d}$ ($M_\odot$)	$r_{\rm dust}$ (au)	$r_{\rm gas}$ (au)	Mass Accretion Rate $\dot{M}$ ($\times 10^{-6}\,M_\odot\,{\rm yr}^{-1}$)	Dust Opacity	Disk Inclination (deg)	Stellar Luminosity ($L_\odot$)
48	(512, 512, 1)	0.30	0.39	60	80	1.2	DSHARP	−70	5.2
49	(512, 512, 1)	0.30	0.39	60	80	0.0	Beckwith	−70	26.0
50	(512, 512, 1)	0.30	0.39	60	80	0.0	Beckwith	−70	5.2
51	(512, 512, 1)	0.30	0.39	60	80	1.5	Beckwith	−70	5.2
52	(512, 512, 1)	0.30	0.39	60	80	1.6	Beckwith	−70	5.2
53	(512, 512, 1)	0.30	0.39	60	80	1.7	Beckwith	−70	5.2
54	(512, 512, 1)	0.30	0.39	60	80	1.8	Beckwith	−70	5.2
55	(512, 512, 1)	0.30	0.39	60	80	1.7	Beckwith	−70	5.2
56	(512, 512, 1)	0.30	0.39	60	80	1.9	Beckwith	−70	5.2
57	(512, 512, 1)	0.30	0.39	60	80	1.9	DSHARP	−70	5.2
58	(512, 512, 1)	0.30	0.39	60	80	1.9	DSHARP	−72	5.2
59	(512, 512, 1)	0.30	0.39	60	80	0.0	Beckwith	−70	5.2
60	(512, 512, 1)	0.30	0.39	60	80	0.0	Beckwith	−70	52.0
61 (Fiducial)	(512, 512, 1)	0.30	0.41	62	80	1.4	DSHARP	−70	5.2
62	(512, 512, 1)	0.30	0.41	62	80	1.4	DSHARP	−72	5.2
63	(512, 512, 1)	0.30	0.41	62	80	1.4	Beckwith	−70	5.2
64	(512, 512, 1)	0.30	0.41	62	80	1.4	OH5	−70	5.2
65	(512, 512, 1)	0.30	0.41	62	80	1.4	Semenov03	−70	5.2
66	(512, 512, 1)	0.30	0.41	62	80	0.0	DSHARP	−70	5.2
67	(512, 512, 1)	0.30	0.41	62	80	0.0	DSHARP	−70	26.0
68	(512, 512, 1)	0.30	0.41	62	80	0.0	Beckwith	−70	5.2
69	(512, 512, 1)	0.30	0.41	62	80	0.0	Semenov03	−70	5.2
70	(512, 512, 1)	0.30	0.41	62	80	0.0	OH5	−70	5.2
71	(512, 512, 1)	0.30	0.45	60	80	1.9	Beckwith	−70	5.2
72	(512, 512, 1)	0.30	0.45	60	80	1.9	DSHARP	−70	5.2
73	(512, 512, 1)	0.30	0.55	62	80	1.4	DSHARP	−70	5.2
74	(512, 512, 1)	0.30	0.60	62	62	1.4	DSHARP	−70	5.2
75	(512, 512, 1)	0.30	0.60	60	60	1.4	Beckwith	−70	5.2
76	(512, 512, 1)	0.30	0.60	80	80	1.4	DSHARP	−70	5.2
77	(512, 512, 1)	0.30	0.60	60	60	1.9	Beckwith	−70	5.2
78	(512, 512, 1)	0.30	0.68	62	80	1.4	DSHARP	−70	5.2
79	(512, 512, 1)	0.30	0.80	60	60	1.4	OH5	−70	5.2
80	(512, 512, 1)	0.30	0.80	60	60	1.4	Semenov03	−70	5.2
81	(256, 256, 1)	0.35	0.06	60	80	4.0	Beckwith	−70	5.2
82	(512, 512, 1)	0.35	0.27	62	80	1.4	DSHARP	−70	5.2
83	(512, 512, 1)	0.35	0.32	60	80	1.9	Beckwith	−70	5.2
84	(512, 512, 1)	0.35	0.39	60	80	1.4	Beckwith	−70	5.2
85	(512, 512, 1)	0.35	0.41	62	80	1.4	DSHARP	−70	5.2
86	(512, 512, 1)	0.35	0.55	62	80	1.4	DSHARP	−70	5.2
87	(256, 256, 1)	0.40	0.03	60	80	5.0	Beckwith	−70	5.2
88	(256, 256, 1)	0.40	0.06	60	80	2.9	Beckwith	−70	5.2
89	(256, 256, 1)	0.40	0.13	60	80	2.3	Beckwith	−70	5.2
90	(256, 256, 1)	0.40	0.19	60	80	2.1	Beckwith	−70	5.2
91	(256, 256, 1)	0.40	0.19	60	80	0.0	Beckwith	−70	5.2
92	(256, 256, 1)	0.40	0.26	60	80	2.2	Beckwith	−70	5.2
93	(512, 512, 1)	0.40	0.27	62	80	1.4	DSHARP	−70	5.2
94	(512, 512, 1)	0.40	0.41	62	80	1.4	DSHARP	−70	5.2

Table 2
(Continued)

Model	Grid (r, θ, ϕ)	Flaring Index, q	$M_{\rm d}$ $(M_\odot)$	$r_{\rm dust}$ (au)	$r_{\rm gas}$ (au)	Mass Accretion Rate $\dot{M}$ $(\times 10^{-6}\ M_\odot\ {\rm yr}^{-1})$	Dust Opacity	Disk Inclination (deg)	Stellar Luminosity $(L_\odot)$
95	(512, 512, 1)	0.45	0.27	62	80	1.4	DSHARP	−70	5.2
96	(256, 256, 1)	0.50	0.06	60	80	3.0	Beckwith	−70	5.2
97	(256, 256, 1)	0.50	0.13	60	80	2.4	Beckwith	−70	5.2
98	(256, 256, 1)	0.50	0.19	60	80	2.0	Beckwith	−70	5.2
99	(256, 256, 1)	0.60	0.06	60	80	3.0	Beckwith	−70	5.2
100 (simobserve)	(512, 512, 1)	0.30	0.41	62	80	1.4	DSHARP	−70	5.2
101 (simobserve)	(512, 512, 1)	0.30	0.41	62	62	1.4	DSHARP	−70	5.2
102 (simobserve)	(512, 512, 1)	0.30	0.41	80	80	1.4	DSHARP	−70	5.2

ORCID iDs

Shigehisa Takakuwa https://orcid.org/0000-0003-0845-128X
Kazuya Saigo https://orcid.org/0000-0003-1549-6435
Miyu Kido https://orcid.org/0000-0002-2902-4239
Nagayoshi Ohashi https://orcid.org/0000-0003-0998-5064
John J. Tobin https://orcid.org/0000-0002-6195-0152
Jes K. Jørgensen https://orcid.org/0000-0001-9133-8047
Yuri Aikawa https://orcid.org/0000-0003-3283-6884
Yusuke Aso https://orcid.org/0000-0002-8238-7709
Sacha Gavino https://orcid.org/0000-0001-5782-915X
Ilseung Han https://orcid.org/0000-0002-9143-1433
Patrick M. Koch https://orcid.org/0000-0003-2777-5861
Woojin Kwon https://orcid.org/0000-0003-4022-4132
Chang Won Lee https://orcid.org/0000-0002-3179-6334
Jeong-Eun Lee https://orcid.org/0000-0003-3119-2087
Zhi-Yun Li https://orcid.org/0000-0002-7402-6487
Zhe-Yu Daniel Lin https://orcid.org/0000-0001-7233-4171
Leslie W. Looney https://orcid.org/0000-0002-4540-6587
Shoji Mori https://orcid.org/0000-0002-7002-939X
Jinshi Sai (Insa Choi) https://orcid.org/0000-0003-4361-5577
Rajeeb Sharma https://orcid.org/0000-0002-0549-544X
Patrick D. Sheehan https://orcid.org/0000-0002-9209-8708
Kengo Tomida https://orcid.org/0000-0001-8105-8113
Jonathan P. Williams https://orcid.org/0000-0001-5058-695X
Yoshihide Yamato https://orcid.org/0000-0003-4099-6941
Hsi-Wei Yen https://orcid.org/0000-0003-1412-893X

References

Añez-López, N., Osorio, M., Busquet, G., et al. 2020, ApJ, 888, 41
Alarcón, F., Casassus, S., Lyra, W., Pérez, S., & Cieza, L. 2024, MNRAS, 527, 9655
Andrews, S. M. 2020, ARA&A, 58, 483
Andrews, S. M., Huang, J., Pérez, L. M., et al. 2018, ApJL, 869, L41
Andrews, S. M., Rosenfeld, K. A., Wilner, D. J., & Bremer, M. 2011, ApJL, 742, L5
Andrews, S. M., Wilner, D. J., Hughes, A. M., et al. 2012, ApJ, 744, 162
Ansdell, M., Williams, J. P., Trapman, L., et al. 2018, ApJ, 859, 21
Armitage, P. 2017, Magnetic Fields and Self-Gravity in Early Protostellar Disks 17-ATP17-107, NASA
Aso, Y., Kwon, W., Ohashi, N., et al. 2023, ApJ, 954, 101
Aso, Y., Ohashi, N., Saigo, K., et al. 2015, ApJ, 812, 27
Aso, Y., & Sai, J. 2023, jinshisai/SLAM: First Release of SLAM, v1.0.0, Zenodo, doi:10.5281/zenodo.7783868
Astropy Collaboration, Price-Whelan, A. M., Lim, P. L., et al. 2022, ApJ, 935, 167
Baek, G., MacFarlane, B. A., Lee, J.-E., et al. 2020, ApJ, 895, 27
Beckwith, S. V. W., Sargent, A. I., Chini, R. S., & Guesten, R. 1990, AJ, 99, 924
Birnstiel, T., Dullemond, C. P., Zhu, Z., et al. 2018, ApJL, 869, L45
Bosman, A. D., Bergin, E. A., Loomis, R. A., et al. 2021, ApJS, 257, 15
Contreras Peña, C., Johnstone, D., Baek, G., et al. 2020, MNRAS, 495, 3614
Crapsi, A., Caselli, P., Walmsley, C. M., et al. 2004, A&A, 420, 957
D'Alessio, P., Cantö, J., Calvet, N., & Lizano, S. 1998, ApJ, 500, 411
Draine, B. T., & Lee, H. M. 1984, ApJ, 285, 89
Dullemond, C. P., 2012 RADMC-3D: A multi-purpose radiative transfer tool, Astrophysics Source Code Library, ascl:1202.015
Facchini, S., van Dishoeck, E. F., Manara, C. F., et al. 2019, A&A, 626, L2
Flores, C., Ohashi, N., Tobin, J. J., et al. 2023, ApJ, 958, 98
Galli, P. A. B., Bouy, H., Olivares, J., et al. 2020, A&A, 634, A98
Ginsburg, A., Robitaille, T., & Beaumont, C., 2016 pvextractor: Position-Velocity Diagram Extractor, Astrophysics Source Code Library, ascl:1608.010
Groppi, C. E., Hunter, T. R., Blundell, R., & Sandell, G. 2007, ApJ, 670, 489
Han, I., Kwon, W., Aso, Y., Bae, J., & Sheehan, P. 2023, ApJ, 956, 9
Hartmann, L., Boss, A., Calvet, N., & Whitney, B. 1994, ApJL, 430, L49
Hu, X., Li, Z.-Y., Zhu, Z., & Yang, C.-C. 2022, MNRAS, 516, 2006
Hughes, A. M., Wilner, D. J., Qi, C., & Hogerheijde, M. R. 2008, ApJ, 678, 1119
Hunter, J. D. 2007, CSE, 9, 90
Ichikawa, T., Kido, M., Takaishi, D., et al. 2021, ApJ, 919, 55
Kido, M., Takakuwa, S., Saigo, K., et al. 2023, ApJ, 953, 190
Kwon, W., Looney, L. W., Mundy, L. G., & Welch, W. J. 2015, ApJ, 808, 102
Lee, C.-F., Li, Z.-Y., Ho, P. T. P., et al. 2017, SciA, 3, e1602935
Lin, Z.-Y. D., Lee, C.-F., Li, Z.-Y., Tobin, J. J., & Turner, N. J. 2021, MNRAS, 501, 1316
Lin, Z.-Y. D., Li, Z.-Y., Yang, H., et al. 2020, MNRAS, 496, 169
Lin, Z.-Y. D., Li, Z.-Y., Yang, H., et al. 2022, MNRAS, 512, 3922
Lin, Z.-Y. D., Li, Z.-Y., Yang, H., et al. 2023a, MNRAS, 520, 1210
Lin, Z.-Y. D., Li, Z.-Y., Tobin, J. J., et al. 2023b, ApJ, 951, 9
Lindberg, J. E., & Jørgensen, J. K. 2012, A&A, 548, A24
Lindberg, J. E., Jørgensen, J. K., Green, J. D., et al. 2014a, A&A, 565, A29
Lindberg, J. E., Jørgensen, J. K., Brinch, C., et al. 2014b, A&A, 566, A74
Liu, S.-F., Jin, S., Li, S., Isella, A., & Li, H. 2018, ApJ, 857, 87
Mathis, J. S., Rumpl, W., & Nordsieck, K. H. 1977, ApJ, 217, 425
McMullin, J. P., Waters, B., Schiebel, D., Young, W., & Golap, K. 2007, in ASP Conf. Ser. 376, Astronomical Data Analysis Software and Systems XVI, ed. R. A. Shaw, F. Hill, & D. J. Bell (San Francisco, CA: ASP), 127
Mendoza, S., Cantó, J., & Raga, A. C. 2004, RMxAA, 40, 147
Momose, M., Ohashi, N., Kawabe, R., Nakano, T., & Hayashi, M. 1998, ApJ, 504, 314
Narayanan, S., Williams, J. P., Tobin, J. J., et al. 2023, ApJ, 958, 20
Ohashi, N., Saigo, K., Aso, Y., et al. 2014, ApJ, 796, 131
Ohashi, N., Tobin, J. J., Jørgensen, J. K., et al. 2023, ApJ, 951, 8
Ossenkopf, V., & Henning, T. 1994, A&A, 291, 943
Panić, O., Hogerheijde, M. R., Wilner, D., & Qi, C. 2009, A&A, 501, 269
Perotti, G., Jørgensen, J. K., Rocha, W. R. M., et al. 2023, A&A, 678, A78
Peterson, D. E., Caratti o Garatti, A., Bourke, T. L., et al. 2011, ApJS, 194, 43
Pinte, C., Dent, W. R. F., Ménard, F., et al. 2016, ApJ, 816, 25
Pringle, J. E. 1981, ARA&A, 19, 137
Robitaille, T. 2019, APLpy v2.0: The Astronomical Plotting Library in Python, v2.0, Zenodo, doi:10.5281/zenodo.2567476
Robitaille, T., & Bressert, E. 2012, APLpy: Astronomical Plotting Library in Python, Astrophysics Source Code Library, ascl:1208.017
Sai, J., Yen, H.-W., Ohashi, N., et al. 2023, ApJ, 954, 67
Schöier, F. L., van der Tak, F. F. S., van Dishoeck, E. F., & Black, J. H. 2005, A&A, 432, 369
Semenov, D., Henning, T., Helling, C., Ilgner, M., & Sedlmayr, E. 2003, A&A, 410, 611
Sharma, R., Jørgensen, J. K., Gavino, S., et al. 2023, ApJ, 954, 69
Tang, Y.-W., Dutrey, A., Koch, P. M., et al. 2023, ApJL, 947, L5
Teague, R. 2019, RNAAS, 3, 74
Teague, R., & Foreman-Mackey, D. 2018, RNAAS, 2, 173
Thieme, T. J., Lai, S.-P., Ohashi, N., et al. 2023, ApJ, 958, 60
Tobin, J. J., van't Hoff, M. L. R., Leemker, M., et al. 2023, Natur, 615, 227
Trapman, L., Facchini, S., Hogerheijde, M. R., van Dishoeck, E. F., & Bruderer, S. 2019, A&A, 629, A79
Ulrich, R. K. 1976, ApJ, 210, 377
van 't Hoff, M. L. R., Tobin, J. J., Trapman, L., et al. 2018, ApJL, 864, L23
van't Hoff, M. L. R., Tobin, J. J., Li, Z.-Y., et al. 2023, ApJ, 951, 10
Villenave, M., Ménard, F., Dent, W. R. F., et al. 2020, A&A, 642, A164
Villenave, M., Stapelfeldt, K. R., Duchêne, G., et al. 2022, ApJ, 930, 11
Yamato, Y., Aikawa, Y., Ohashi, N., et al. 2023, ApJ, 951, 11
Yang, H., & Li, Z.-Y. 2020, ApJ, 889, 15
Yang, H., Li, Z.-Y., Looney, L., & Stephens, I. 2016, MNRAS, 456, 2794
Yang, H., Li, Z.-Y., Looney, L. W., Girart, J. M., & Stephens, I. W. 2017, MNRAS, 472, 373
Yen, H.-W., Takakuwa, S., Ohashi, N., et al. 2014, ApJ, 793, 1
Yoon, S.-Y., Lee, J.-E., Lee, S., et al. 2021, ApJ, 919, 116